

# Intermittent Deployment for Large-Scale Multi-Robot Forage Perception: Data Synthesis, Prediction, and Planning

Jun Liu<sup>1</sup>, Murtaza Rangwala<sup>1</sup>, Kulbir Singh Ahluwalia<sup>2</sup>, Shayan Ghajar<sup>3</sup>, Harnaik Singh Dhama<sup>4</sup>, Pratap Tokekar<sup>4</sup>, Benjamin F. Tracy<sup>5</sup>, and Ryan K. Williams<sup>1</sup>

*Abstract*—Monitoring the health and vigor of grasslands is vital for informing management decisions to optimize rotational grazing in agriculture applications. To take advantage of forage resources and improve land productivity, we require knowledge of pastureland growth patterns that is simply unavailable at state of the art. In this paper, we propose to deploy a team of robots to monitor the evolution of an unknown pastureland environment to fulfill the above goal. To monitor such an environment, which usually evolves slowly, we need to design a strategy for rapid assessment of the environment over large areas at a low cost. Thus, we propose an integrated pipeline comprising of data synthesis, deep neural network training and prediction along with a multi-robot deployment algorithm that monitors pasturelands *intermittently*. Specifically, using expert-informed agricultural data coupled with novel data synthesis in ROS Gazebo, we first propose a new neural network architecture to learn the spatiotemporal dynamics of the environment. Such predictions help us to understand pastureland growth patterns on *large scales* and make appropriate monitoring decisions for the future. Based on our predictions, we then design an intermittent multi-robot deployment policy for low-cost monitoring. Finally, we compare the proposed pipeline with other methods, from data synthesis to prediction and planning, to corroborate our pipeline’s performance.

*Note to Practitioners*—Pasturelands are an integral part of agricultural production in the United States. To take full advantage of the forage resource and avoid environmental degradation, pastureland must be managed optimally. This paper focuses on the question of how to deploy robot teams to sense and model physical processes over varying timescales. The goal of this work is to develop a new integrated pipeline for long-term deployment of heterogeneous robot teams grounded in the problem of autonomous monitoring in precision grazing to improve land productivity. By using the proposed pipeline in grassland ecosystem management, we will have a better understanding of the physical environment while respecting energy budgets.

*Index Terms*—Precision agriculture, intermittent deployment, planning, spatiotemporal prediction, deep learning.

This work was supported by the National Institute of Food and Agriculture under Grant 2018-67007-28380.

<sup>1</sup>The authors are with the Department of Electrical and Computer Engineering, Virginia Tech, Blacksburg, VA 24061 USA (e-mail: junliu@vt.edu; murtazar@vt.edu; rywilli1@vt.edu).

<sup>2</sup>The author is with the Department of Agriculture and Biological Engineering, University of Illinois, Urbana-Champaign, IL 61801 USA (e-mail: ksa5@illinois.edu).

<sup>3</sup>The author is with the Department of Crop and Soil Science, Oregon State University, Corvallis, OR 97331 USA (e-mail: ghajars@oregonstate.edu).

<sup>4</sup>The author is with the Department of Computer Science, University of Maryland, College Park, MD 20782 USA (e-mail: dhama@umd.edu; tokekar@umd.edu).

<sup>5</sup>The author is with the School of Plant and Environmental Sciences, Virginia Tech, Blacksburg, VA 24061, USA (e-mail: bfracy@vt.edu).

## I. INTRODUCTION

Grasslands provide many ecosystem services such as livestock production, wildlife habitat, water infiltration, and carbon sequestration [1]. Consequently, monitoring the health and vigor of grasslands is vital for informing management decisions to protect or optimize these ecosystem services [2]. Sward or canopy height data provide valuable insights into the productivity, habitat value, or maturity of grasslands. When sward height data are monitored over time, changes in sward height can indicate whether a grassland is deteriorating, maintaining its vigor, or becoming more productive. In agricultural systems, monitoring height data can inform decisions about the appropriate timing and intensity of grazing in order to meet economic and ecological goals.

Traditional methods of measuring aboveground height or aboveground biomass rely on labor-intensive methods [3]. For height, this necessitates measuring canopy height by hand using a meter stick or Robel pole [4]. Aboveground biomass measurements often consist of destructive harvest of forage. Samples are usually cut by hand from a quadrat or frame, bagged, then dried in a forced-air forage oven until reaching a constant weight, known as the dry matter. Depending on the size of the pasture or scope of the monitoring project, height and biomass sampling may involve dozens or hundreds of such samples to ensure that the collected data represents the entirety of the pasture or landscape being monitored. Advancements in proximal sensing technologies can provide accurate measurements of height and biomass predictions faster and over larger areas than these labor-intensive traditional methods. However, regular field measurements from pastures through remote sensing methods such as Unmanned Aerial Vehicles (UAVs) are constrained by multiple factors such as limited spatial coverage and low frequency of UAV deployments. Moreover, adverse weather conditions and other resource constraints also contribute to limited deployment and consequently insufficient field measurements of the pasture required to plan grazing activities. In spite of these limitations, precision agriculture involving the use of UAVs to monitor the growth of crops is a promising approach to covering large areas in reasonable times. Analyzing point clouds obtained from the LiDAR attached to UAVs can help to determine the spatial distribution of plants, growth in different regions of the farm and consequently help the farmer focus their resources in regions where they are required the most. Developing prediction models for pastures

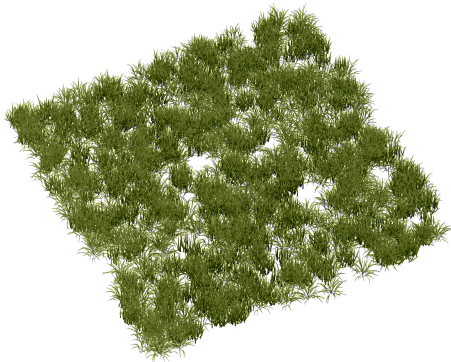


**Fig. 1** A patch ( $2\text{m} \times 2\text{m}$ ) of the simulated pastureland with a density of 250 grass models per square meter.

that work within the limitation of UAV deployment schedules is a promising approach and helps alleviate resource-limited field measurements. Additionally, motivation for this methodology can be found in related applications such as lost-person search and rescue, where powerful predictive models and UAV teams have shown great promise in large-scale efforts [5], [6]. Overall, we argue that an intermittent robot deployment scheme coupled with a tightly integrated prediction and planning model would generate maximum efficiency for livestock grazing and pasture recovery processes.

With the above motivation, this paper explores the use of autonomous robots to facilitate environmental monitoring for improving land productivity. At a high level, our proposed pipeline works as follows (Fig. 2). We first use historical data to synthesize a 3D dynamic field to simulate the spatiotemporal environmental process of the site that needs to be monitored (Section IV). For illustration, a small patch ( $2\text{m} \times 2\text{m}$ ) of the generated pasture is shown in Fig. 1, where the density is 250 grass models per square meter. We then use this data to train neural networks to learn the dynamics of this field (Section V). Then, an intermittent deployment policy is designed for multi-robot teams (UAVs in our case) using the future pasture height predictions while respecting system budgets (Section VI). After that, we simulate a pastureland environment in ROS Gazebo [7] to test the performance of the synthesized data (Section VII). Finally, we evaluate the performance of each aspect of our solution and compare it to competing methods (Section VIII).

In order to synthesize appropriate training data for high-quality predictions, historical data were generated using the expert-informed Agricultural Production Systems sIMulator (APSIM) Next Generation in Section IV. APSIM is designed to model long-term agricultural production in a variety of systems [8]. Using historical meteorological data from three sites in Iowa, APSIM simulated 30 years of tall fescue (*Schedonorus arundinacea*) pasture dry matter production for each site. Simulated pasture yield was then used to generate average pasture height data based on the equation reported by Schaefer and Lamb [9] describing the relationship between pasture green dry matter and LiDAR-measured pasture height. Based on the historical average pasture height data, we then use a Gaussian mixture model (GMM) to simulate the dynamics of this field over the desired monitoring horizon in Section IV.

Even with a sufficient training data set based on expert-informed historical data, developing an effective prediction model for estimating pasture growth is challenging due to changes incurred by the climate and the spatiotemporal characteristics of the growth. Previous studies for forecasting spatiotemporal dependencies have been based on conventional approaches. These methods require a complex and meticulous simulation of the physical environment for a particular application. Instead, machine learning-based models provide increased flexibility in tackling the difficult spatiotemporal sequence prediction problem that large-scale forage monitoring poses. To address this problem from a deep learning perspective, we use our proposed long short-term memory (LSTM) and convolutional neural network (CNN) based architecture [10] to model the pasture growth forecasting problem in Section V.

Finally, with high-quality pasture growth predictions, a multi-robot deployment policy can be designed to guide future field measurements, as detailed in Section VI. Our proposed deployment policy aims to maximize the sum of collected information (uncertainty) from the environment while considering waiting penalties and energy constraints of the system. In general, we formulate this deployment problem as a submodular maximization problem [11] with matroid constraints [12]. The energy constraints will be formulated as matroid constraints, while the collected information and the waiting penalties will be part of our objective function. Additionally, as the deployment policies gather field measurements, the prediction model can be updated iteratively to generate more accurate estimates of future pasture growth. Through an optimized prediction and deployment model, we show that UAV deployments for pasture monitoring can be scheduled based on the prediction model instead of regular intervals, effectively reducing the required number of deployments. This *need-based intelligent* deployment policy substantially reduces the cost of gathering field measurements and effectively allows resource-constrained enterprises to manage pasture grazing more effectively.

Beyond the forage monitoring problem, the proposed pipeline can be mapped to other large-scale monitoring problems for sufficiently slow spatiotemporal processes where intermittent deployment is reasonable. That is, the data synthesis – neural network training/prediction – intermittent multi-robot deployment pipeline is quite general, given access to expert-informed data as a starting point. For example, in ocean monitoring applications [13], [14], we can also use the proposed pipeline to generate and refine deployment policies given the availability of high-quality models of aquatic processes.

*Contributions:* In summary, the contributions of this work are as follows:

- We propose an integrated pipeline<sup>1</sup> to simulate and solve an important problem in the precision agricultural space, forage monitoring, including data synthesis, prediction, planning, and perception (Section III).
- We demonstrate how to exploit historical agricultural data to synthesize a pastureland environment in a manner that accommodates both neural network training and rapid prototyping in a simulation environment (Section IV).

<sup>1</sup><https://github.com/precision-grazing/project>

- We demonstrate a scalable spatiotemporal learning architecture that can be used to integrate with an intermittent multi-robot planning strategy (Section V).
- We introduce a novel intermittent deployment policy that integrates neural network-based predictions while considering budgets to deploy robots for autonomous environmental monitoring (Section VI).
- We have built (and made available) a high-fidelity pastureland simulation environment in ROS Gazebo, allowing for rapid prototyping of pasture monitoring with LiDAR point clouds (Section VII).

## II. RELATED WORK

Predictive modeling of agricultural systems can provide helpful information on their long-term resilience and productivity. Predictive models have been developed for many crops and regions, tested extensively, and refined for increased predictive accuracy for commodities such as corn, soybeans, wheat and rice, to name a few. As model accuracy increases, it can provide insights into crop responses to abiotic stressors such as climate change [15], [16], or identify optimal crop rotations between species over a period of years [17]. However, agricultural modeling of forage systems presents unique challenges compared to row cropping systems, as forage systems are often perennial rather than annual, the forage crop can be “harvested” multiple times per year by grazing livestock or cutting for hay, and pastures are typically multispecies ecosystems rather than monospecific crops with homogeneous phenotypes and physiology [18]. Several forage modeling programs have been developed despite the aforementioned challenges. These include—but are not limited to—the Simulation of Production and Utilization on Rangelands (SPUR) first developed on rangelands in the 1980s [19]; the GRAzing SIMulation Model (GRASIM) developed in the late 1990s [20]; the Dairy Forage System Model (DAFOSYM) developed in the late 1980s and updated into the Integrated Farm System Model (IFSM) [21]; and the Agricultural Production Systems sIMulator (APSIM) Next Generation, which can model both row-cropping systems and pastures [22]. We select APSIM as the optimal modeling program for our research, as the program has been used previously for pasture modeling in a variety of contexts [23], [24]; provides daily timestep outputs which fulfilled our need for fine-grained temporal data; and the program’s modular nature allows for rapid customization of input parameters [16], [25].

The problem of predicting an evolving pastureland over time may be solved with conventional methods such as Gaussian processes (GPs) [26], which focus on stochastic Gaussian processes to model the regression for different pasture heights or observations. This method is also known as Kriging [26]. GPs are non-parametric methods by defining the internal relations between observations [27]. Similarly, Gaussian Markov Random Fields (GMRFs) are often used to model spatial environmental fields [26]. These conventional methods are suitable for problems where there is significant prior knowledge of the environment that needs to be monitored. The historical data used in this paper can give us a general

trend of the average height change of the field. However, as we must make predictions on large scales, this prior is insufficient for us to generate a reasonable conventional model for the entire pastureland environment (not to mention the issues with computational scaling). Moreover, as the growth patterns may differ across the field, conventional models are not as flexible for modeling the heterogeneity of growth patterns spatially and temporally. We, therefore, sought to apply a neural network-based method to tackle this prediction problem when we have a large dataset for modeling the heterogeneity of the environment.

Specifically, we implement a framework that integrates a neural network-based encoder-decoder architecture to learn the historical data’s underlying patterns over time for future predictions. The problem of predicting future pasture heights is analogous to video frame prediction [28], with the key challenge in our case lying in predicting the growth of pasture surfaces. In the deep learning-based prediction domain, sequence-to-sequence problems were originally introduced through recurrent neural networks (RNN) and long short-term memory (LSTM) models and provide a baseline for solving temporal forecasting problems that we encounter in this work [29]–[31]. To incorporate spatial features, prior works have generally used multiple architectures to consider spatial and temporal features separately by combining the autoencoder or a generative adversarial network (GAN) model with an RNN model [28], [32], [33]. Convolutional LSTMs (ConvLSTMs) [34] have been successfully used for spatiotemporal predictive learning and were originally proposed for precipitation nowcasting over radar images. Recent works have used the architecture for learning frame representations [35]. Motion-content network (MCNet) [36] uses an additional LSTM apart from the image encoder to model the motion dynamics. The outputs of both the encoders are combined and fed to the decoder to predict frames. Recently, [37], [38] proposed ST-LSTM to learn structural information for spatiotemporal sequences and a new model structure PredRNN and PredRNN++ to explicitly decouple memory cells and improve the cross-layer interaction of memory states across different LSTMs. These methods help improve stronger spatial correlation and short-term dynamics for powerful modeling and prediction capabilities. We utilize the recent developments in ConvLSTM applications and propose a novel prediction architecture that is particularly effective in predicting the rapidly changing dynamics of the pasture over long horizons. We achieve this through the use of recurrent encoder-decoder networks based on ConvLSTMs over different resolutions of the pasture to effectively capture different features and dependencies of the pasture dynamics. Moreover, by using appropriate processing described in Section V over raw pasture data, our pasture terrain forecasting technique can scale to any terrain size.

Standard learning-based models do not capture model uncertainty. Unlike regression problems where a model can output a predictive probability, as we deal with a sequence-to-sequence prediction problem, we need to extrapolate prediction uncertainty from training data. Bayesian probability theory has been used in deep learning as a tool to deal with uncertainty [39], [40], where the weights of the neural network are

defined as distributions. Bayesian neural networks (BNN) are more robust to over-fitting. However, they add significant computation complexity. Sampling-based and stochastic variational inference methods have been used to approximate Bayesian neural networks [41]–[44]. Similar to BNN, these methods incur high computational costs without additional benefits to improving accuracy. An alternative approach [45] with minimal computational and model complexity in deep learning models was proposed through the use of Dropouts [46]. The authors show that any neural network with arbitrary depth and non-linearities, modeled with dropouts behind every layer, is equivalent to the approximation of a probabilistic deep Gaussian process [47]. In our previous work [10], we integrate this concept of uncertainty estimation from dropout over our architecture to provide the necessary uncertainty maps for multi-robot monitoring from a typical machines learning perspective. Whereas in this work, our focus is about integrating a combinatorial optimization based planner with proposed deep learning based predictions [10] and performing a deep evaluation of the entire pipeline with realistic simulations. From the multi-robot deployment perspective, to estimate the evolving processes of pastureland environments more efficiently, we cannot deploy robots (UAVs) to collect observations frequently because it is not energy efficient. Those types of observations can be point clouds, heightmaps, sonar data, etc. Meanwhile, the deployment strategy should be generated based on environmental information instead of being artificially defined. This intermittent idea can also be found in other robotics applications. In [48], the robots in a team are designed to communicate intermittently while working together to explore an environment. In [49], the authors use time windows to model the availability of robots at different times in task allocation applications. Therefore, robots are not required to work continuously. The idea of intermittence is contrary to that of persistence, where robots are required to work continuously to fulfill different tasks [50], [51]. In [52], the authors proposed a deep learning-based method for combining environmental prediction and path planning, where the spatial path planning is the main concern in the paper. In [53], the authors investigated a sampling-based path planning method for variance reducing. Similarly, in [54], the author used an adaptive sampling strategy for reducing entropy generated from GP modeling. In [55], a GMRF-based method was proposed for spatial predictions.

Since the monitored environment evolves spatially and temporally, we need to utilize the predicted environmental information to make a spatiotemporal deployment plan. In [56], we use a partially observable Markov decision process (POMDP) to model the dynamics of an environmental process. Then, a submodular objective function is applied to model the false alarm and delay cost. This method works only when the process models are known and can be modeled as POMDPs. In [57], [58], we use non-parametric Gaussian processes [26] to model the dynamics of a monitored environmental process and then use mutual information as a metric to guide our deployments. Meanwhile, matroids are used to model the budget constants. Generally speaking, matroids [11], [12] can be used to model the independence in constraints, which can be found in many robotics applications, e.g., task allocation

[59], multi-robot deployment [60], topology selection and planning [61], and probabilistic security/resilience in multi-robot systems [62], [63], etc. We will also use this tool to model the independence of different constraints in the deployment strategy in this work. In general, the environmental modeling methods used in our previous works are conventional GP-based methods, where a prior of the entire environment is needed to utilize historical data. While in this paper, the environment modeling method is a data-driven approach, which builds the dynamics of the environment through a historical dataset where an exact process model is not required. Moreover, the environment modeling and the deployment policy generation are highly connected in this paper. Finally, as the deployment policies gather more measurements, the proposed data-driven prediction model can be updated accordingly for better future predictions.

### III. PRELIMINARIES AND PROBLEM FORMULATION

#### A. Preliminaries

A core aspect of this paper is to optimize multi-robot deployment plans by utilizing historical agricultural data. We propose to tackle this problem from a combinatorial optimization perspective. To this end, we begin by reviewing the concepts related to our objective function and constraint modeling.

A set function  $f : 2^{\mathcal{V}} \mapsto \mathbb{R}$  is a function that maps any set  $\mathcal{A} \subseteq \mathcal{V}$  into  $\mathbb{R}$ , where  $\mathcal{V}$  is the finite discrete ground set of  $f(\cdot)$ .

*Definition 1 ([11]):* A set function  $f : 2^{\mathcal{V}} \mapsto \mathbb{R}$  is

- normalized, if  $f(\emptyset) = 0$ ;
- monotone non-decreasing, if  $f(\mathcal{A}) \leq f(\mathcal{B})$  when  $\mathcal{A}, \mathcal{B} \subseteq \mathcal{V}$ , and  $\mathcal{A} \subseteq \mathcal{B}$ ;
- submodular, if  $f(\mathcal{A} \cup \{v\}) - f(\mathcal{A}) \geq f(\mathcal{B} \cup \{v\}) - f(\mathcal{B})$  when  $\mathcal{A}, \mathcal{B} \subseteq \mathcal{V}$ ,  $\mathcal{A} \subseteq \mathcal{B}$ , and  $v \in \mathcal{V} \setminus \mathcal{B}$ .

The property of *submodularity* is often described as having a diminishing returns property (as the above definition suggests), making it a natural option for modeling objective functions in robotics (e.g., sensor placement [64], set coverage [11], task allocation [65]). It is also convenient to work with the *marginal return* when an element  $v$  is added to  $\mathcal{A}$ , which is defined as  $f(\{v\} | \mathcal{A}) = f(\mathcal{A} \cup \{v\}) - f(\mathcal{A})$ . The submodularity level of a set function can be measured using curvature, a property of the set function itself. Curvature can be defined as follows.

*Definition 2 ([66]):* Let  $f : 2^{\mathcal{V}} \mapsto \mathbb{R}$  be a monotone non-decreasing submodular function, we define the curvature of  $f(\cdot)$  as

$$c_f = \max_{v \in \mathcal{V}} \frac{f(\mathcal{V}) - f(\mathcal{V} \setminus \{v\})}{f(v)},$$

where  $\mathcal{V}$  is the ground set.

It holds that  $0 \leq c_f \leq 1$ . If  $c_f = 0$ , then  $f(\cdot)$  is a modular function and  $f(\mathcal{A} \cup \{v\}) - f(\mathcal{A}) = f(v)$ ,  $\forall \mathcal{A} \subseteq \mathcal{V}$ ,  $v \in \mathcal{V} \setminus \mathcal{A}$  when  $\mathcal{V}$  is the ground set. If  $c_f = 1$ , then  $f(\mathcal{A} \cup \{v\}) - f(\mathcal{A}) = 0$ , where  $\mathcal{A} \subseteq \mathcal{V}$  and  $v \in \mathcal{V} \setminus \mathcal{A}$ . This means adding  $v$  has no contribution to the function value  $f(\cdot)$  if set  $\mathcal{A}$  is selected.

Next, we introduce the related concept of constraint modeling. Matroids generalize the idea of independence in set systems.



Meanwhile, efficient sub-optimal solutions can be found when constraints are modeled by matroids [67].

*Definition 3 ([12]):* A matroid  $\mathcal{M} = (\mathcal{V}, \mathcal{I})$  is a set system that contains a finite ground set  $\mathcal{V}$  and a collection  $\mathcal{I}$  of subsets of  $\mathcal{V}$  with the following properties:

- 1)  $\emptyset \in \mathcal{I}$ ;
- 2) If  $\mathcal{A} \subseteq \mathcal{B} \in \mathcal{I}$ , then  $\mathcal{A} \in \mathcal{I}$ ;
- 3) If  $\mathcal{A}, \mathcal{B} \in \mathcal{I}$  and  $|\mathcal{B}| < |\mathcal{A}|$ , there exists a  $v \in \mathcal{A} \setminus \mathcal{B}$  such that  $\mathcal{B} \cup \{v\} \in \mathcal{I}$ .

The intersection of  $L$  matroids can be written as  $\mathcal{M} = (\mathcal{V}, \mathcal{I})$ , where  $\mathcal{M}_i = (\mathcal{V}, \mathcal{I}_i)$  is the  $i$ th matroid and  $\mathcal{I} = \bigcap_{i=1}^L \mathcal{I}_i$ . The cardinality of this matroid intersection constraint is  $|\mathcal{M}| = L$ . A set belonging to a matroid means that this set should satisfy the matroid conditions. Examples of matroid constraint modeling in robotics can be found in task allocation [59], orienteering [68], action selection [69], etc.

## B. Problem Formulation

Consider a spatiotemporal forage process evolving in a 2D pasture environment (which we model rigorously in the sequel). In simple terms, we are interested in determining forage height for any location in the pasture environment over a long time horizon by deploying multi-robot teams. To fulfill this goal, we divide our efforts into two tasks: forage process prediction and multi-robot planning. In the following, we outline the fundamentals of these tasks and conclude with a concrete problem statement.

*a) Prediction:* Assume that we are given historical 2D heightmaps  $\mathbf{X}_t \in \mathbb{R}^{M \times N}$  of a pasture field at different times, where  $t$  is the associated time index, and  $M, N$  are the width and the length of the pasture heightmap, which correspond to the discretization resolution. This resolution will be used for both the prediction problem and the planning problem. Denote by  $\mathcal{X} = \{\mathbf{X}_t \in \mathbb{R}^{M \times N} \mid t \in \mathcal{T}_x\}$  the historical dataset containing all the historical measurements, where  $\mathcal{T}_x$  contains all the time indexes associated with each  $\mathbf{X}_t \in \mathcal{X}$ . The extracted height of the pasture in location  $(x, y)$  with respect to  $\mathbf{X}_t$  is denoted by  $\mathbf{X}_t(x, y)$ . Our first goal is to train a neural network to predict future pasture heights  $\bar{\mathbf{Y}}_t$  for the prediction horizon  $\mathcal{T}_y$  using the historical dataset  $\mathcal{X}$ . This prediction process is modeled as

$$(\bar{\mathbf{Y}}_t, \bar{\sigma}_t^2) \leftarrow \Theta(\mathcal{X}, \mathbf{W}), \quad \forall t \in \mathcal{T}_y, \quad (1)$$

where  $\Theta$  is our neural network model,  $\mathbf{W}$  is the set of parameters of the model,  $\bar{\mathbf{Y}}_t \in \mathbb{R}^{M \times N}$  is the predicted heightmap at  $t$ , and  $\bar{\sigma}_t^2 \in \mathbb{R}^{M \times N}$  is the corresponding variance at  $t$ . Also, we denote by  $\bar{\mathcal{Y}} = \{\bar{\mathbf{Y}}_t \in \mathbb{R}^{M \times N} \mid \forall t \in \mathcal{T}_y\}$  the prediction set that contains all of the predicted heightmaps for the prediction horizon  $\mathcal{T}_y$ , and denote by  $\bar{\Sigma} = \{\bar{\sigma}_t^2 \in \mathbb{R}^{M \times N} \mid \forall t \in \mathcal{T}_y\}$  the corresponding variance set. The details will be specified in Section V.

*b) Planning:* Based on the predicted heightmaps  $\bar{\mathcal{Y}}$  and variance maps  $\bar{\Sigma}$ , we seek a multi-robot deployment strategy to collect data, reinforce our predictions, and ultimately make better pastureland management decisions. To determine a deployment strategy, we first need to build the ground set  $\mathcal{V}$ , which contains all possible deployment decisions for robots

over space and time. Consider a team of robots available to deploy over the time horizon  $\mathcal{T}_y$ , the prediction horizon. The family of all available locations is denoted by  $\mathcal{P}$ . Thus, we have  $(x, y) \in \mathcal{P}$ , and  $|\mathcal{P}| = M \cdot N$  is the cardinality of the deployable locations. We also denote by  $\mathcal{R}$  the set of indices of all robots. Each robot  $r \in \mathcal{R}$  may have a different sensing ability, i.e., sensing noise. Therefore, the ground set  $\mathcal{V}$  at time  $t$ , containing all available deployment choices, is as follows:

$$\mathcal{V}_t = \{(x, y, r, t) : \forall (x, y) \in \mathcal{P}, r \in \mathcal{R}, t \in \mathcal{T}_y\}.$$

We interpret  $(x, y, r, t)$  as “location  $(x, y)$  is sensed by robot  $r$  at time  $t$ ”. To simplify the notation, we will use a 4-tuple  $v := (x, y, r, t)$  to denote the deployment decision factor in the following. Finally, the ground set of the deployment problem is  $\mathcal{V} = \bigcup_{t \in \mathcal{T}_y} \mathcal{V}_t$ . The cardinality of the ground set is  $|\mathcal{V}| = |\mathcal{P}| \cdot |\mathcal{R}| \cdot |\mathcal{T}_y|$ . The associated predicted variance with respect to  $v$  at  $t$  is represented by  $\bar{\sigma}_t^2(v), \forall v \in \mathcal{V}$ . Since  $\bar{\sigma}_t^2(v)$  is the predicted variance map at time  $t$  for  $v$ , we can use  $\bar{\sigma}_t^2(x, y) \in \mathbb{R}$  to denote the predicted variance that corresponds to location  $(x, y) \in \mathcal{P}$  at time  $t \in \mathcal{T}_y$ . We want to determine a deployment policy set  $\mathcal{S} \in \mathcal{V}$  to maximize the information we can get from the environment while respecting the system budgets. To this end, we denote by  $f : 2^{\mathcal{V}} \mapsto \mathbb{R}$  the objective function, and denote by  $\mathcal{M}$  a set of sets defining the system’s admissible deployment policies. The details will be specified in Section VI.

*c) Problem Statement:* With the basics of prediction and planning outlined, we now formalize the problem we solve in this paper.

*Problem 1 (Intermittent Deployment):* Consider a historical set  $\mathcal{X} = \{\mathbf{X}_t \in \mathbb{R}^{M \times N} \mid \forall t \in \mathcal{T}_x\}$ , containing heightmaps of a discretized  $M \times N$  pasture over a time horizon  $\mathcal{T}_x$ . Let  $\mathcal{V}$  be the ground set containing all possible multi-robot deployment factors  $v := (x, y, r, t)$  over a time horizon  $\mathcal{T}_y$ . Assume further the existence of a predicted variance set  $\bar{\Sigma} = \{\bar{\sigma}_t^2 \in \mathbb{R}^{M \times N} \mid \forall t \in \mathcal{T}_y\}$ . The intermittent deployment problem is maximize a set function  $f(\cdot)$  by selecting appropriate deployment factors while respecting budget constraints. That is,

$$\begin{aligned} & \underset{\mathcal{S} \subseteq \mathcal{V}}{\text{maximize}} && f(\mathcal{S}) \\ & \text{subject to} && \mathcal{S} \in \mathcal{M}. \end{aligned}$$

By selecting the set  $\mathcal{S}$  that maximizes the objective function, we can determine all deployment factors containing deployment locations and times to conduct deployments while maintaining efficiency.

*Remark 3.1:* This work focuses on predictions and planning perspectives, especially in spatiotemporal deployment locations selection under limited energy conditions. We should note that a path planning problem is a subsequent problem of our framework, and any of them can be integrated into our framework. Therefore, we focus on prediction and planning to set up a cornerstone for the subsequent problems.

The diagram of our proposed solution to the above problem is shown in Fig. 2. Our pipeline can be divided into the following aspects, which we detail in the sequel: data synthesis (Section IV), deep learning prediction (Section V), planning (Section VI), and Gazebo evaluation (Section VII).

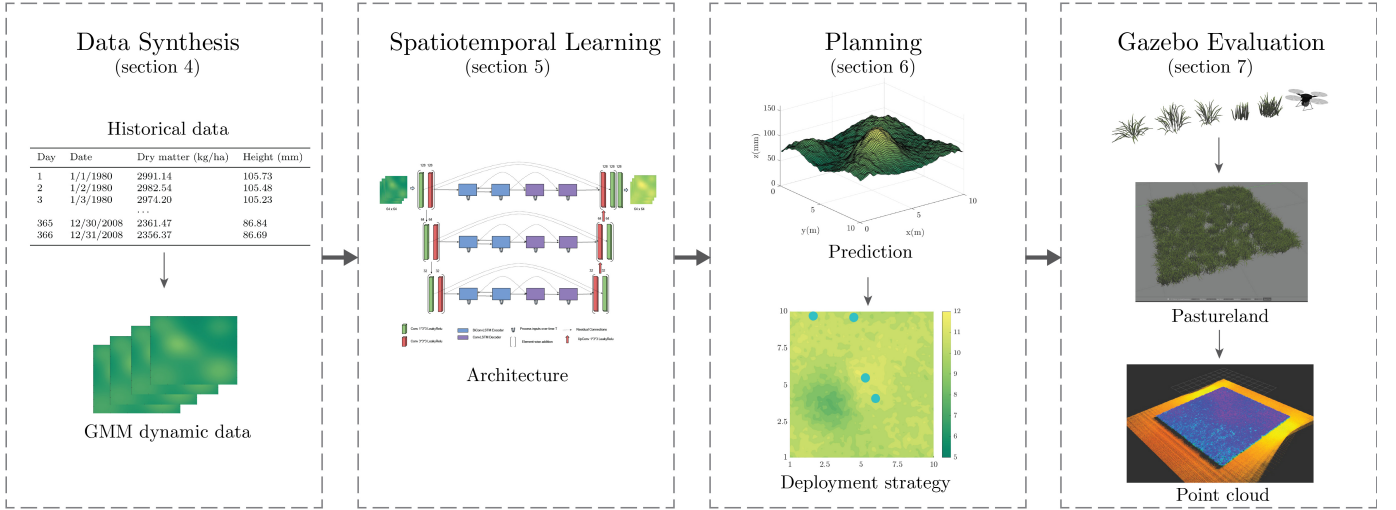


**Fig. 2** A diagram of our overarching solution. Data synthesis is first used to simulate historical pasture data. Then spatiotemporal learning is used for neural network training and prediction based on historical data. Next, the planning aspect is used to make multi-robot deployment decisions for collecting new data. Finally, on the far right we illustrate the high-fidelity simulation we have built for evaluating our pipeline.

#### IV. LARGE-SCALE PASTURE ENVIRONMENT SYNTHESIS

In this section, we focus on pasture environment synthesis. This process will be divided into two parts. First, we illustrate how to synthesize historical average pasture height data (Section IV-A). Based on this data, we then introduce how to utilize this data to create a dynamic pasture environment (Section IV-B).

##### A. Historical Data Preparation

‘Historic’ pasture data were generated using APSIM Next Generation’s publicly available meteorological, soils, and pasture species modules. We selected three sites in Iowa due to the availability of meteorological data for each in APSIM’s Met module as a result of prior research [70]. Meteorological data spanned 1979 to 2013 and included solar radiation ( $\text{MJ}/\text{m}^2$ ), rain and snowfall, minimum and maximum temperature, atmospheric pressure, and day length. Soils selected in the module were fine-loamy, mixed, superactive, mesic Hapludolls common in Iowa, also available in APSIM’s modules [70]. APSIM’s tall fescue AgPasture module was used for the forage species [16]. Tall fescue was set to 1m rooting depth and initial belowground and aboveground biomass of 1000 kg/ha and 3000 kg/ha, respectively. The SoilOM module, which simulates soil organic matter processes, was set to 1000 kg/ha initial surface residue. Fertilizer application was simulated at 84 kg N/ha on January 1 and another 84 kg N/ha on August 15 each year in the form of nitrate ( $\text{NO}_3\text{-N}$ ). The resulting simulated pasture yield was then used to generate average pasture height data using an equation reported by Schaefer and Lamb [9] describing the relationship between LiDAR-measured pasture height and pasture green dry matter, i.e., green aboveground biomass. In this paper, we denote by  $\mathbf{h} \in \mathbb{R}^{\mathcal{T}_x}$  the historical data, where  $\mathcal{T}_x = |\mathcal{T}_x|$  is the length of the historical dataset horizon  $\mathcal{T}_x$ , which is also defined in the problem formulation in Section III-B. We also denote by  $\mathbf{h}_t \in \mathbb{R}$  the average pasture height data at time  $t$  in the historical dataset. Further information on the above APSIM

modules’ functions and processes may be found in the work of Li and colleagues [16].

##### B. Pasture Environment Data Synthesis

The generated average pasture height data is temporal data. When making predictions for different locations and developing spatiotemporal deployment strategies, we need both spatial and temporal historical data to know the different growth patterns in different places of the pasture field. Therefore, this section focuses on synthesizing spatiotemporal data from the historical average pasture height data. In general, this process fits a spatiotemporal process to the temporal aspects of the historical data.

In this work, we use a dynamic Gaussian mixture model (GMM), a combination of Gaussian distributions, to simulate the pasture evolution using historical data. The GMM used in this work is a discrete model as we need to make predictions for different days and make corresponding deployment decisions for different times and locations. We should note that there are many other ways to simulate a spatiotemporal process by using temporal data only, and we select GMM for the following reasons. GMM is a common tractable process representation, which allows us to adjust the model to match the actual field evolving process. From expert inputs or manual field measurements, we can choose reasonable spatial parameters for the GMM to complement the temporal parameters coming from historical data, so the spatiotemporal model represents the pasture evolving process.

In general, we first use  $B$  components to build a dynamic GMM and then use the historical data  $\mathbf{h}$  to adjust the generated model to match the historical information. The dynamic GMM is model as

$$\mathbf{G}_t(x, y) = \sum_{i=1}^B w_i(t) b_i(x, y) = \mathbf{w}(t)^\top \mathbf{b}(x, y), \quad (2)$$

where  $(x, y) \in \mathbb{R}^2$  is a 2D location from the location set  $\mathcal{P}$ , basis  $b_i(x, y) \in \mathbb{R}$  is the output of  $i$ th basis function in

the location  $(x, y)$ ,  $B$  is the number of basis functions, and  $\mathbf{G}_t(x, y)$  is the output of the GMM at time  $t$  and location  $(x, y)$ . The weight  $w_i(t) \in \mathbb{R}$  is associated with  $b_i(x, y)$ , where  $t \in \mathcal{T}_x$ . The  $i$ th basis function  $b_i(x, y)$  is a Gaussian kernel function. That is,

$$b_i(x, y) = \exp\left[-\frac{[(x, y) - (b_{xi}, b_{yi})]^2}{2c_i^2}\right], \quad (3)$$

where  $(b_{xi}, b_{yi}) \in \mathbb{R}^2$  is the 2D position of  $i$ th basis function  $b_i(x, y)$ , and  $c_i$  is the corresponding length-scale. Also,  $\mathbf{w}(t) \in \mathbb{R}^B$  is the stacked weights at time  $t$  and  $\mathbf{b}(x, y) \in \mathbb{R}^B$  is the stacked basis functions for the location  $(x, y)$ . One way to generate a dynamic 3D smooth surface to simulate pasture is to change the weights of different basis functions smoothly at different times. To achieve this goal, we use a 1D Gaussian process [71] to model the change of each weight at different times for the entire time horizon  $\mathcal{T}_x$ . After this step, a dynamic GMM is fully built.

Next, we need to adjust this model to make its temporal property match the historical average height data. Specifically, we need to adjust the generated GMM surfaces at different times using the historical average height data. That is:

$$\mathbf{X}_t(x, y) \leftarrow \mathbf{G}_t(x, y) + \mathbf{h}_t - \bar{\mathbf{G}}_t,$$

where  $\mathbf{h}_t \in \mathbb{R}$  is the historical average height at time  $t$ , and  $\bar{\mathbf{G}}_t \in \mathbb{R}$  is the simulated average height of the field at that time, which is calculated by using  $\bar{\mathbf{G}}_t = |\mathcal{P}|^{-1} \sum_{(x, y) \in \mathcal{P}} \mathbf{G}_t(x, y)$ . After this adjustment, the averaged height of the generated surfaces at different times meets the historical data. Meanwhile, those surfaces' heights, i.e.,  $\mathbf{X}_t(x, y)$ , are truncated if the height is negative. Finally, small noise is added to the surfaces to simulate a diversified growth pattern in the pasture. After this series of operations, the spatiotemporal dataset  $\mathcal{X} = \{\mathbf{X}_t \in \mathbb{R}^{M \times N} \mid t \in \mathcal{T}_x\}$  is fully constructed and can be used in the later learning and predictions.

To summarize the data synthesis process, we first synthesize the historical average data  $\mathbf{h}$ . Then, we build a dynamic GMM denoted by  $\mathbf{G}$ , and adjust this model to make the temporal property of  $\mathbf{G}$  match the historical average data  $\mathbf{h}$ . Finally, the adjusted dataset is denoted by  $\mathcal{X}$  that will be used in learning and predictions (below).

## V. SPATIOTEMPORAL LEARNING AND PREDICTION

In this section, we will be first focusing on learning the dynamics of the generated field using the generated dataset  $\mathcal{X} = \{\mathbf{X}_t \in \mathbb{R}^{M \times N} \mid t \in \mathcal{T}_x\}$ . Note that a pre-processing will be applied before feeding  $\mathcal{X}$  into our training networks. Then, we will use the learned dynamics to make predictions of the field for the future, which will then serve as inputs for the deployment strategy planning (Section VI).

In general, our spatiotemporal learning network is modeled as

$$(\bar{\mathbf{Y}}_t, \bar{\sigma}_t^2) \leftarrow \Theta(\mathcal{X}, \mathbf{W}), \quad \forall t \in \mathcal{T}_y,$$

where  $\Theta$  is our neural network model,  $\mathbf{W}$  is the set of parameters of the model,  $\bar{\mathbf{Y}}_t \in \mathbb{R}^{M \times N}$  is the predicted heightmap at  $t$ , and  $\bar{\sigma}_t^2 \in \mathbb{R}^{M \times N}$  is the corresponding variance

at  $t$ . Next, we give the details of our mean and variance predictions.

Since the prediction model will take as input a sequence of heightmaps to predict multi-step long-horizon future pasture heights, we need to reorganize  $\mathbf{X}_t \in \mathcal{X}, \forall t \in \mathcal{T}_x$  to satisfy this requirement. Meanwhile, we need pre-processing to enable our proposed model to tackle different pasture sizes. We aim to reorganize all  $\mathbf{X}_t \in \mathcal{X}, \forall t \in \mathcal{T}_x$  to form multiple training sequences. We define the  $i$ th training sequence as  $\mathcal{X}_i = \{\mathbf{X}_t \in \mathbb{R}^{M \times N} \mid \forall t \in \mathcal{T}_i\}$  with  $\mathcal{T}_i = \{i, i + \delta, \dots, i + \alpha\delta\}$ , where  $\delta$  is the number of intervals before each input observation in the training sequence,  $\alpha$  is the number of observations in  $\mathcal{X}_i$ , and  $\mathcal{T}_i$  contains all the time index associated with every  $\mathbf{X}_t \in \mathcal{X}_i$ . Note that  $\mathcal{T}_i \subseteq \mathcal{T}_x$ . The complementary training label (ground truth) for an input sequence  $\mathcal{X}_i$  is then defined as  $\mathcal{Y}_i = \{\mathbf{Y}_t \in \mathbb{R}^{M \times N} \mid \forall t \in \mathcal{T}_y\}$ , where  $\mathcal{T}_y = \{i + (\alpha + 1)\delta, i + (\alpha + 2)\delta, \dots, i + (2\alpha + 1)\delta\}$  contains the expected prediction step at  $\delta$  intervals. Therefore,  $\alpha = |\mathcal{T}_i| = |\mathcal{T}_y|$ . The effective length (horizon) of the input and output sequences are then calculated as  $L = \delta \cdot \alpha$ . Varying the number of strides  $\delta$  in the sequences allows our prediction model to work with both short term and long term horizon. For example, given a input sequence of  $\alpha = 15$  and a stride of  $\delta = 4$ , we have an effective observation length of 60 days. Finally, the neural network outputs a prediction sequence  $\bar{\mathbf{Y}}_i = \{\bar{\mathbf{Y}}_t \in \mathbb{R}^{M \times N} \mid \forall t \in \mathcal{T}_y\}$  for each input sequence  $\mathcal{X}_i$ , where  $\bar{\mathbf{Y}}_t$  is the prediction with respect to the ground truth  $\mathbf{Y}_t$  at  $t$ .

*Remark 5.1:* For the scope of this paper, we train our networks using the same input and output observation interval  $\delta$  and the same number of observation/measurements  $\alpha$ . That is,  $\alpha = |\mathcal{T}_i| = |\mathcal{T}_y|$ . However, it is to be noted that the proposed network can be trained on varying sequence lengths without changing the architectural design. This is due to the inherent flexibility of an encoder-decoder design.

The high-level idea of the mean predictions is as follows. For each time  $t$ , we will use the averaged prediction  $\bar{\mathbf{Y}}_t$  from several Monte Carlo (MC) predictions  $\hat{\mathbf{Y}}_t^{(k)} \in \mathbb{R}^{M \times N}$  as the final predicted heightmap at  $t$ , where  $\hat{\mathbf{Y}}_t^{(k)}$  is the  $k$ th MC prediction at time  $t$ . That is,  $\hat{\mathbf{Y}}_t^{(k)} \leftarrow \Theta(\mathcal{X}, \mathbf{W}), \forall t \in \mathcal{T}_y$ .

The averaged mean prediction is given by

$$\bar{\mathbf{Y}}_t := \mathbb{E}_{\text{Pr}(\bar{\mathbf{Y}}_t | \mathcal{X})}(\bar{\mathbf{Y}}_t) \approx \frac{1}{K} \sum_{i=1}^K \hat{\mathbf{Y}}_t^{(k)}, \quad \forall t \in \mathcal{T}_y. \quad (4)$$

Each MC prediction is a realization of the proposed network by using a different setting, which will be specified later, and the number of sampled predictions is  $K$  for each heightmap prediction  $\bar{\mathbf{Y}}_t, \forall t \in \mathcal{T}_y$ .

Our network architecture is shown in Fig. 3. We adapt the ubiquitous U-Net Convolution Neural Network framework [72] with ConvLSTM cells as an encoder-decoder framework for making sequence predictions. We introduce a novel architecture, where the model learns spatiotemporal dependencies for long-horizon predictions using a mixture of Convolutional Neural Networks (CNN) and ConvLSTM encoder-decoder layers.

We can now define the process that allows the architecture to capture spatiotemporal dependencies. As a first step, we define the ConvLSTM architecture [34] that forms a building

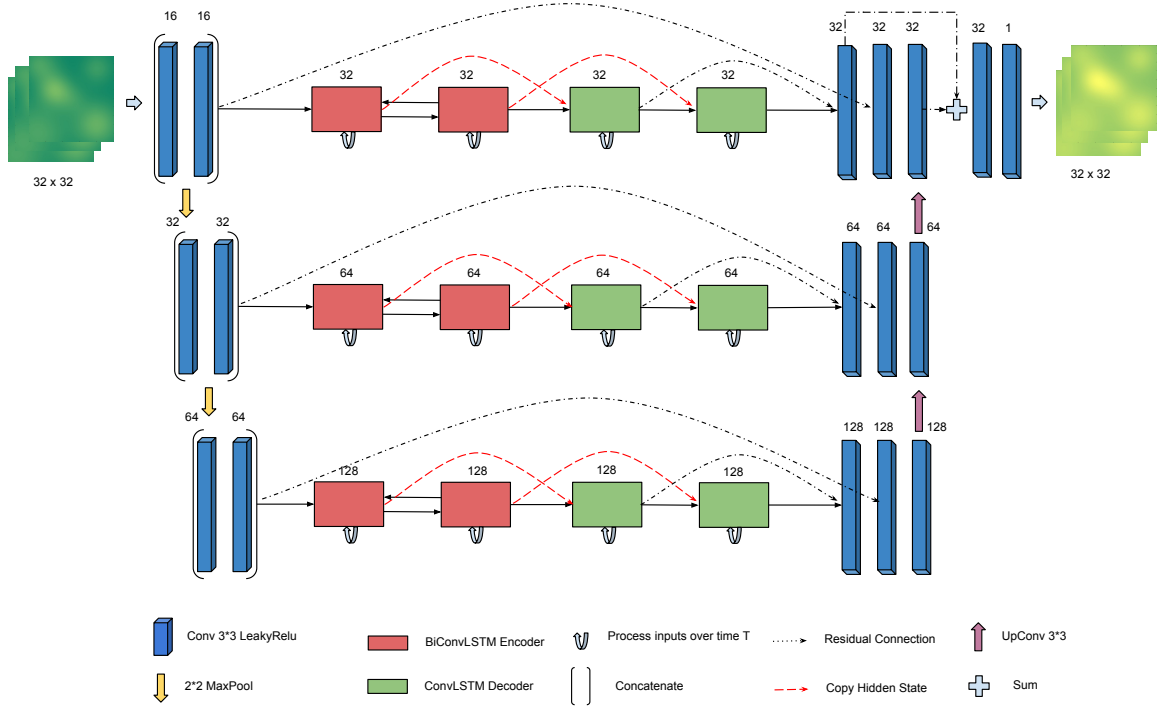


**Fig. 3** Prediction neural network architecture is defined as an encoder-decoder. Initial feature maps across different resolutions are generated using Conv2D encoders and then are iteratively fed to the ConvLSTM encoders to encode the input observations. The ConvLSTM decoders then recursively generate representations for each interval in the output. These recurrent hidden representations across resolutions are then merged to generate the final sequence of prediction. Residual connections are used to ease regeneration of outputs from the generated hidden representations.

block for our model. ConvLSTMs can be seen as a special case of LSTMs, by replacing the Hadamard product in LSTMs with convolution operators. The ConvLSTM block enables the network to recursively process a sequence of representations and update its hidden states  $\mathbf{H}_t$  that encode the complete spatiotemporal representations for all  $\mathcal{X}_i$ 's. The key idea behind ConvLSTMs is its capability to *retain* information that is relevant to its prediction task, and *forget* information over time that might be repetitive or not necessary over the sequence. The operations within the ConvLSTM block is shown as follows:

$$\begin{aligned}
 \mathbf{I}_t &= \varphi(\mathbf{W}_{xi} * \mathbf{X}_t^c + \mathbf{W}_{hi} * \mathbf{H}_{t-1} + \mathbf{W}_{ci} \circ \mathbf{C}_{t-1} + \mathbf{W}_i), \\
 \mathbf{F}_t &= \varphi(\mathbf{W}_{xf} * \mathbf{X}_t^c + \mathbf{W}_{hf} * \mathbf{H}_{t-1} + \mathbf{W}_{cf} \circ \mathbf{C}_{t-1} + \mathbf{W}_f), \\
 \mathbf{D}_t &= \mathbf{I}_t \circ \tanh(\mathbf{W}_{xc} * \mathbf{X}_t^c + \mathbf{W}_{hc} * \mathbf{H}_{t-1} + \mathbf{W}_c), \\
 \mathbf{C}_t &= \mathbf{F}_t \circ \mathbf{C}_{t-1} + \mathbf{D}_t, \\
 \mathbf{O}_t &= \varphi(\mathbf{W}_{xo} * \mathbf{X}_t^c + \mathbf{W}_{ho} * \mathbf{H}_{t-1} + \mathbf{W}_{co} \circ \mathbf{C}_t + \mathbf{W}_o), \\
 \mathbf{H}_t &= \mathbf{O}_t \circ \tanh(\mathbf{C}_t),
 \end{aligned}$$

where  $*$  denotes the convolution operation,  $\circ$  is the Hadamard product,  $\mathbf{X}_t^c \in \mathbb{R}^{D \times W \times H}$  is the input of the ConvLSTM block at time  $t$ ,  $D$  is the number of stacked heightmaps in the blocks,  $\mathbf{H}_t \in \mathbb{R}^{D \times W \times H}$  is the hidden state and also the output of the block at  $t$ ,  $\mathbf{F}_t \in \mathbb{R}^{W \times H}$  is a gate that controls what information needs to be forgotten or retained for the next step,  $\mathbf{O}_t \in \mathbb{R}^{W \times H}$  is an output gate that controls what information is passed on to the hidden state,  $\mathbf{D}_t, \mathbf{C}_t \in \mathbb{R}^{D \times W \times H}$  are the temporary cell state and the cell state at time  $t$  that work to accumulate the information over the history of the sequence,  $\varphi: \mathbb{R}^{W \times H} \mapsto$

$\mathbb{R}^{W \times H}$  is a sigmoid function. Finally,  $\mathbf{W}_\bullet \in \mathbb{R}^{W \times H}$  are the learnable weights and biases of the network.

Formally, we define the model uncertainty through dropouts in the neural network by sampling  $K$  different sets of parameters  $\mathbf{W}_\bullet$ . That is,

$$\bar{\sigma}_t^2 = \text{Var}(\hat{\mathbf{Y}}_t^{(k)}), \quad \forall t \in \mathcal{T}_y.$$

This operation is equivalent to performing  $K$  stochastic forward passes with the dropout of weights enabled during inference and then averaging the results. In this work, we simulate the MC dropout sampling by using the  $\text{Pr} = 0.4$  probability of dropping each weight set for stochastic inference during prediction. Through the use of dropouts between each layer in our network, both during training and testing time, we enable our encoder-decoder model to estimate the prediction set  $\bar{\mathcal{Y}} = \{\bar{\mathbf{Y}}_t \in \mathbb{R}^{M \times N} \mid \forall t \in \mathcal{T}_y\}$  and the corresponding variance set  $\bar{\Sigma} = \{\bar{\sigma}_t^2 \in \mathbb{R}^{M \times N} \mid \forall t \in \mathcal{T}_y\}$ . The MC dropout method allows our model to generate the requisite prediction estimates and the uncertainty on its prediction in a computationally efficient process. Therefore, a more detailed network model showing our intermediate outputs, i.e.,  $\hat{\mathbf{Y}}_t$  and  $\hat{\sigma}_t^2$ , can be summarized as

$$(\bar{\mathbf{Y}}_t, \bar{\sigma}_t^2) \leftarrow (\hat{\mathbf{Y}}_t, \hat{\sigma}_t^2) \leftarrow \Theta(\mathcal{X}, \mathbf{W}), \quad \forall t \in \mathcal{T}_y.$$

We also refer the reader to [10] for more details about our mean and variance predictions. After the spatiotemporal learning of the pasture, we are ready to make predictions for the horizon  $\mathcal{T}_y$ .

## VI. MULTI-ROBOT INTERMITTENT DEPLOYMENT

The goal of the deployment to maximize the information we can get from the environment while respecting the budgets. To this end, we model the objective function  $f : 2^{\mathcal{V}} \mapsto \mathbb{R}$  as follows:

$$f(\mathcal{S}) = \sum_{s \in \mathcal{S}} \left( \bar{\sigma}_t^2(s) \sum_{s' \in \mathcal{S} \setminus s} \frac{d(s, s')}{|\mathcal{S} \setminus s|} \right) - w_1(t - t_1), \quad (5)$$

where  $\bar{\sigma}_t^2(s)$  is the prediction variance of the decision factor  $s$  at time  $t$ . Note that  $t_1$  is the starting time index of the prediction horizon  $\mathcal{T}_y$ . The distance function  $d(s, s')$  is the weighted Euclidean distance and time difference between  $s$  and  $s'$ . That is,

$$d(s, s') = w_2 \log(\|(x, y) - (x', y')\|) + w_3 |t - t'|, \quad (6)$$

where  $s = (x, y, r, t)$  and  $s' = (x', y', r', t')$  are two different decision factors. And  $w_1$  is the waiting penalty weight,  $w_2$  is the weight for the physical distance, and  $w_3$  is the weight for the time difference between  $s$  and  $s' \in \mathcal{S} \setminus s$ .

The objective function is a weighted sum of prediction variances. The nominator  $\bar{\sigma}_t^2(s)$  is the prediction variance of the decision factor  $s$  at time  $t$ . The denominator is the sum of the weighted distances between  $s$  and  $s' \in \mathcal{S} \setminus s$  for all  $s \in \mathcal{S}$ . Meanwhile,  $w_1$  is the weight to penalize the waiting time. We can deploy robots using a deployment set  $\mathcal{S}$  that maximizes the objective function  $f(\cdot)$  to reduce the prediction uncertainty.

Since the deployment should be energy efficient, we have two constraints to model the deployment budgets. The first constraint is,

$$|\mathcal{S} \cap \mathcal{V}_t| \leq \ell_t, \forall t \in \mathcal{T}_y. \quad (7)$$

This constraint (per-day budget) indicates that the number of deployments cannot be larger than  $\ell_t$  at time  $t$ , where  $\ell_t \in \mathbb{R}$ . The second constraint is,

$$\sum_{t \in \mathcal{T}_y} \mathbb{1}(\mathcal{S} \cap \mathcal{V}_t) \leq \ell, \quad (8)$$

where  $\mathbb{1}(\cdot)$  is an indicator function as

$$\mathbb{1}(|\mathcal{S} \cap \mathcal{V}_t|) = \begin{cases} 1, & \text{if } |\mathcal{S} \cap \mathcal{V}_t| \geq 1, \\ 0, & \text{if } |\mathcal{S} \cap \mathcal{V}_t| = 0. \end{cases}$$

This constraint (total budget) suggests that the total number of deployable days cannot be larger than  $\ell$ , where  $\ell \in \mathbb{R}$ . Therefore, the details of our problem formulation is

$$\begin{aligned} & \underset{\mathcal{S} \subseteq \mathcal{V}}{\text{maximize}} && f(\mathcal{S}, \bar{\Sigma}) \\ & \text{subject to} && |\mathcal{S} \cap \mathcal{V}_t| \leq \ell_t, \forall t \in \mathcal{T}_y \\ & && \sum_{t \in \mathcal{T}_y} \mathbb{1}(\mathcal{S} \cap \mathcal{V}_t) \leq \ell. \end{aligned}$$

It has been shown that both constraints are matroidal [57], and we will use  $\mathcal{M}_1 = (\mathcal{V}, \mathcal{I}_1)$  and  $\mathcal{M}_2 = (\mathcal{V}, \mathcal{I}_2)$  to denote those two, where  $\mathcal{M}_1, \mathcal{M}_2$  are matroids and  $\mathcal{I}_1, \mathcal{I}_2$  are independent sets. To simplify the notation, we use  $\mathcal{M} = (\mathcal{V}, \mathcal{I})$ , where  $\mathcal{I} = \mathcal{I}_1 \cap \mathcal{I}_2$ , to denote the intersection of two constraints. Thus,  $\mathcal{M}$  is a matroid intersection constraint and the cardinality is  $|\mathcal{M}| = 2$ .

---

**Algorithm 1** The algorithm for the long-term pasture prediction and sensing problem.

---

**Input:** The inputs are as follows:

- The historical dataset  $\mathcal{X} = \{\mathbf{X}_t \in \mathbb{R}^{M \times N} \mid \forall t \in \mathcal{T}_x\}$ ;
- The neural network  $\Theta(\cdot)$ ;
- The deployment ground set  $\mathcal{V}$ ;
- The objective function  $f : 2^{\mathcal{V}} \mapsto \mathbb{R}$ ;
- The matroid intersection constraint  $\mathcal{M} = (\mathcal{V}, \mathcal{I})$ .

**Output:** The deployment strategy set  $\mathcal{S}$ .

---

```

1: for  $t \in \mathcal{T}_y = \{\tau, \dots, T\}$  do
2:    $\hat{\mathbf{Y}}_t^{(k)} \leftarrow \Theta(\mathcal{X}, \mathbf{W}), \forall k = 1, \dots, K;$ 
3:    $\bar{\mathbf{Y}}_t \leftarrow \frac{1}{K} \sum_{k=1}^K \hat{\mathbf{Y}}_t^{(k)};$  ▷ Mean
4:    $\bar{\sigma}_t^2 \leftarrow \text{Var}(\hat{\mathbf{Y}}_t^{(k)});$  ▷ Variance
5:    $\bar{\Sigma} \leftarrow \bar{\Sigma} \cup \{\bar{\sigma}_t^2\};$ 
6: end for
7:
8:  $\mathcal{S} \leftarrow \emptyset, \mathcal{Z} \leftarrow \mathcal{V};$ 
9: while  $\mathcal{Z} \neq \emptyset$  do
10:   $s \in \arg \max_{v \in \mathcal{V} \setminus \mathcal{Z}} f(\{v\} \mid \mathcal{S});$ 
11:  if  $\mathcal{S} \cup \{s\} \in \mathcal{I}$  then
12:     $\mathcal{S} \leftarrow \mathcal{S} \cup \{s\};$ 
13:  end if
14:   $\mathcal{Z} \leftarrow \mathcal{Z} \cup \{s\};$ 
15: end while
16:  $\mathcal{S} \leftarrow$  deployment strategy;

```

---

Using the proposed architecture with ConvLSTM and residual connections, we have the predicted variance set  $\bar{\Sigma} = \{\bar{\sigma}_t^2 \in \mathbb{R}^{M \times N} \mid \forall t \in \mathcal{T}_y\}$ . Given the intermittent deployment problem (Problem 1) and the deployment ground set  $\mathcal{V}$ , we propose to solve the problem using Algorithm 1. From lines 1-6, we first use the proposed architecture to predict the variance set  $\bar{\Sigma}$  for the prediction time set  $\mathcal{T}_y$ . In the second part, the algorithm greedily selects all the available decision factors  $v \in \mathcal{V} \setminus \mathcal{Z}$  based on the marginal gain  $f(\{v\} \mid \mathcal{S})$ , where  $\mathcal{Z}$  is used to store all checked decision factors. The set  $\mathcal{S}$  is current solution of the deployment strategy and will be updated iteratively. Specifically, we initialize a set  $\mathcal{Z}$  as  $\mathcal{V}$ . Then, in line 10, we select one of the decision factors  $v$  that maximizes the marginal gain of the objective function  $f(\{v\} \mid \mathcal{S})$ , where  $\mathcal{S}$  is the current solution of the problem and will be expanded as more decision factors are checked. In lines 11-13, we need to check if  $v$  satisfies the matroidal deployment constraint  $\mathcal{M} = (\mathcal{V}, \mathcal{I})$ . If so,  $v$  is added to the solution set  $\mathcal{S}$  as  $\mathcal{S} \leftarrow \mathcal{S} \cup \{s\}$ . Otherwise, the next round will be started. Meanwhile,  $\mathcal{Z}$  is updated to store the checked decision factor  $v$  as  $\mathcal{Z} \leftarrow \mathcal{Z} \cup \{s\}$ . The iteration will be finished when every decision factor in  $\mathcal{V}$  is checked against the constraint  $\mathcal{M} = (\mathcal{V}, \mathcal{I})$ .

If we define the optimal deployment policy of the intermittent deployment problem as  $\mathcal{S}^*$  with respect to the predicted variance set  $\bar{\Sigma}$ , we then have the following result.

*Theorem 1 ([66]):* The optimality ratio of the greedy solution



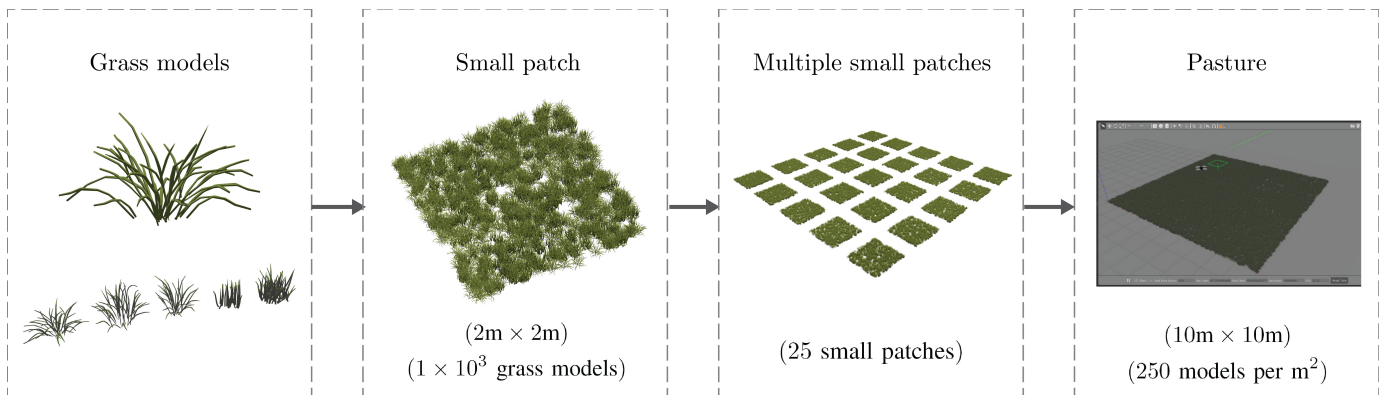


Fig. 4 A diagram of our pasture construction process.

$\mathcal{S}$  generated by Algorithm 1 has the following performance:

$$f(\mathcal{S}) \geq \frac{1}{|\mathcal{M}| + c_f} f(\mathcal{S}^*) = \frac{1}{2 + c_f} f(\mathcal{S}^*),$$

where  $c_f$  is the curvature of  $f(\cdot)$ ,  $|\mathcal{M}| = 2$  is the cardinality of the matroid intersection constraint, and  $\mathcal{S}^*$  is an optimal solution.

The above result gives a lower bound of algorithm Algorithm 1 for our problem. Note that the curvature of the objective function  $f(\cdot)$  can be evaluated by checking the contribution of every decision factor  $v$  from the ground set  $\mathcal{V}$  as shown in Definition 2. Therefore, by using the proposed Algorithm 1, we can get an intermittent deployment policy using the proposed method while having a performance guarantee, as shown above.

*Remark 6.1:* The proposed pipeline can also be implemented in a receding horizon manner. That is, based on the proposed deployment policy  $\mathcal{S}$ , the new robot measurements from a series of deployments can be integrated into the historical dataset  $\mathcal{X}$  to refine the learned network  $\Theta(\cdot)$ . Therefore, we can produce better predictions  $(\bar{\mathbf{Y}}_t, \bar{\sigma}_t^2)$  and thus improved plans  $\mathcal{S}$  for the future.

## VII. PASTURE CONSTRUCTION AND PERCEPTION

When we have a synthesized pasture, we need a representation of what aerial robots with LiDAR would measure. Thus, we simulate a realistic pasture environment and LiDAR measurements in Gazebo based on our synthesized data. This high-fidelity pastureland simulation environment will help us to understand the effectiveness of the simulated process. In this section, we will first focus on constructing pasture environments from the simulated data and then on the height estimation using LiDAR measurements.

*Pasture construction:* In this work, we simulate a 10m x 10m pasture using  $2.5 \times 10^4$  grass models. We set the size of the simulated pasture and the density like this when considering the computational complexity. First, we randomly pick  $2.5 \times 10^4$  locations from this pastureland environment. We then assign a 3D grass model in each sampled location. The heights of grass models correspond to the heights at the same locations in the smooth 3D surfaces. To accelerate the simulation speed and lower the computational requirement, we divide the pasture into 25 small patches (2m x 2m per patch). In each patch, the

density is 250 grass models per square meter with a total of  $1 \times 10^3$  models per small patch. In this small patch, we use five species of plants to simulate different growth patterns as shown in Fig. 4. This selection will be validated later in the experimental section as the actual measurements look similar to our simulated environment. Each plant is spawned at the same randomly chosen coordinates throughout our simulation. We rescale a grass model in each dimension for each randomly selected location according to the desired height in the 3D surface. The flowchart of our pasture construction is shown in Fig. 4.

*Pasture perception:* To estimate the height of the pasture, we use a UAV equipped with a LiDAR to collect point clouds over the pasture. Meanwhile, we need post-processing to remove noise after getting the point clouds. Those extra points are not part of the simulated field and need to be removed. To achieve this, we use crop box filters to remove the extra points and retain the points of the 10m x 10m pasture as well as the points in the perimeter around it. The height of a point cloud includes two parts: the height of pasture and the height of the ground plane. To get the estimated height of the field, we use the mowed-down perimeter to estimate the ground plane. First, we have the following assumption of the ground of the environment.

*Assumption 1 (Ground Plane):* We assume that the ground of the pastureland is a plane.

In the simulation, we use this assumption to facilitate the ground height estimation. However, other types of ground can also be integrated into our simulation framework, where we can use more sophisticated methods for ground surface regression.

In this work, we use the least squares method to compute the height of the ground by using perimeter points. The perimeter is all the points surrounding the target plot area. These perimeter points will be used to estimate the ground plane that is used for height estimation. An equation for a plane can be defined as shown below.

$$Ax + By + Cz + D = 0. \quad (9)$$

where  $A, B, C$ , and  $D$  are the parameters defining the plane. Without loss of generality, we assume  $C = 1$ . We denote by  $\mathbf{p}_i = [x_i, y_i, z_i]^T \in \mathbb{R}^3$  the location of  $i$ th point in the perimeter. Since we are solving for a best-fit plane of multiple

**TABLE I** The locations, length-scales, and initial weights of different basis functions.

$i$	Location $(x, y)$	Length-scale $c_i$	Initial weight $w_i$
1	(5.0, 5.0)	0.13	4.17
2	(3.0, 4.0)	0.13	4.17
3	(2.0, 1.5)	0.15	2.50
4	(8.0, 8.0)	0.18	6.67
5	(8.0, 1.5)	0.13	3.33
6	(1.0, 1.0)	0.13	3.33
7	(1.0, 9.0)	0.25	4.17

points, a least square form of our formulation can be written as

$$\begin{bmatrix} x_1 & y_1 & 1 \\ x_2 & y_2 & 1 \\ \dots & \dots & \dots \\ x_P & y_P & 1 \end{bmatrix} \begin{bmatrix} A \\ B \\ D \end{bmatrix} = - \begin{bmatrix} z_1 \\ z_2 \\ \dots \\ z_P \end{bmatrix},$$

where  $P$  is the total number of points in the perimeter.

To perform the linear least squares test, we multiple a transpose of the left-most matrix on both sides. Note that we will use  $\sum x_i x_i$  as  $\sum_{i=1}^P x_i x_i$  for simplicity. This notation will also be applied to other relevant terms. Then the above equation is simplified as

$$\begin{bmatrix} \sum x_i x_i & \sum x_i y_i & \sum x_i \\ \sum y_i x_i & \sum y_i y_i & \sum y_i \\ \sum x_i & \sum y_i & P \end{bmatrix} \begin{bmatrix} A \\ B \\ D \end{bmatrix} = - \begin{bmatrix} \sum x_i z_i \\ \sum y_i z_i \\ \sum z_i \end{bmatrix}.$$

Defining all points, i.e.,  $\mathbf{p}_i = [x_i, y_i, z_i]^T$ , relative to the plane centroid sets the summations of the individual components to 0 and simplifies the above equations. The centroid of the plane is calculated by using  $\mathbf{o} = P^{-1} \sum_{i=1}^P \mathbf{p}_i \in \mathbb{R}^3$ . Note that  $P \neq |\mathcal{P}|$ . Then, all the points in the perimeter are updated as  $[x_i, y_i, z_i]^T \leftarrow [x_i, y_i, z_i]^T - \mathbf{o}$ . The above equation can then be simplified as

$$\begin{bmatrix} \sum x_i x_i & \sum x_i y_i & 0 \\ \sum y_i x_i & \sum y_i y_i & 0 \\ 0 & 0 & P \end{bmatrix} \begin{bmatrix} A \\ B \\ D \end{bmatrix} = - \begin{bmatrix} \sum x_i z_i \\ \sum y_i z_i \\ 0 \end{bmatrix}.$$

From the last row, we observe that  $D = 0$  since  $P \neq 0$ . Therefore, this equation can further be simplified as

$$\begin{bmatrix} \sum x_i x_i & \sum x_i y_i \\ \sum y_i x_i & \sum y_i y_i \end{bmatrix} \begin{bmatrix} A \\ B \end{bmatrix} = - \begin{bmatrix} \sum x_i z_i \\ \sum y_i z_i \end{bmatrix}.$$

Using Cramer's rule, we get  $A$  and  $B$  as follows.

$$\begin{aligned} A &= (\sum y_i z_i \times \sum x_i y_i - \sum x_i z_i \times \sum y_i y_i) / \Delta, \\ B &= (\sum x_i y_i \times \sum x_i z_i - \sum x_i x_i \times \sum y_i z_i) / \Delta, \end{aligned} \quad (10)$$

where

$$\Delta = \sum x_i x_i \times \sum y_i y_i - \sum x_i y_i \times \sum x_i y_i.$$

Therefore, the ground plane is fully defined, and the actual height of the pastureland can be adjusted accordingly.

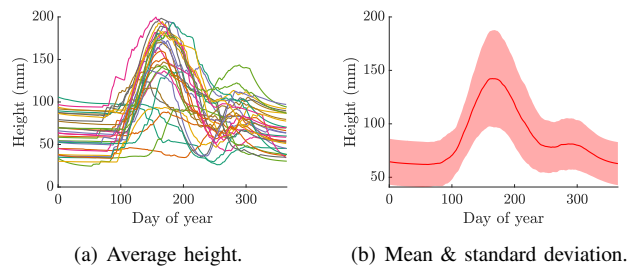


**Fig. 5** (a). The average height of the pastureland environment in 30 years (represented by 30 lines). The x-axis represents the day of a year. The y-axis represents the corresponding average height. (b). The mean and the standard deviation of the height of each day are calculated by using the historical data.

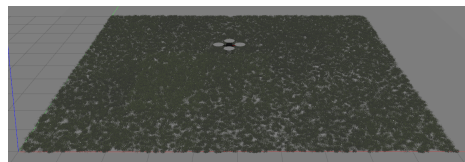


**Fig. 6** A simulated pastureland 10m  $\times$  10m environment using  $2.5 \times 10^4$  grass models

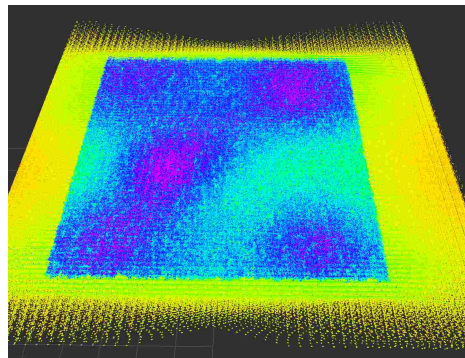


**Fig. 7** The corresponding point cloud of the pasture (10m  $\times$  10m) shown in Fig. 6.

## VIII. EVALUATION

In this section, we demonstrate the results of each component in our pipeline. The historical data is generated using Matlab. The pasture is simulated by using Blender. The neural network training was conducted with a PyTorch backend on a 2x AMD Epyc 7742 CPUs and a multi-GPU training regime with 8x Nvidia RTX 6000 GPUs.

### A. Data Preparation

Based on historical meteorological data from a site in Iowa, we simulate 30 years of tall fescue pasture dry matter production. Specifically, we will use the first 28 years data for training and reserve the last year's data for testing purposes. In Fig. 5, we demonstrate the statistics of the historical data. Fig. 5(a) shows the average height change of the simulated pastureland environment, where each line denotes the height change for different days in a year. We also calculate the mean and the standard deviation for each day using the historical data as shown in Fig. 5(b).

The simulated pasture yield was then used to generate average pasture height data based on the model in [9] describing

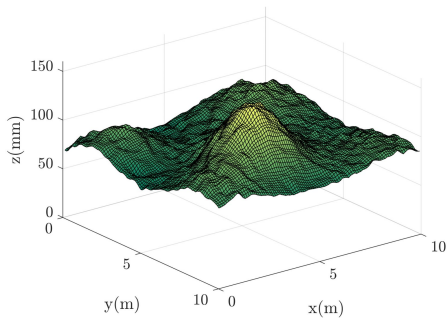


**Fig. 8** The downsampled surface of the point cloud shown in Fig. 7.

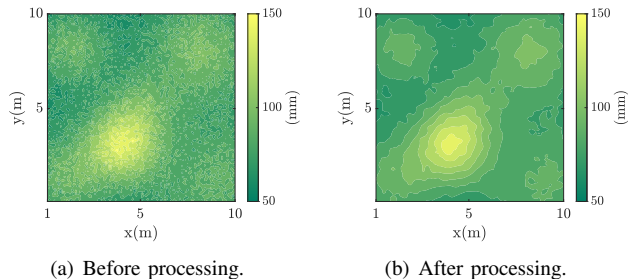


**Fig. 9** The downsampled heightmaps of the point cloud shown in Fig. 7.

the relationship between pasture green dry matter and LiDAR-measured pasture height for each day. Following the pastureland generation procedure described in Section IV-B, we generate a pastureland environment using a dynamic GMM. In the simulation, we use  $B = 7$  basis functions. The random initial settings of the basis function location  $(x, y)$ , the length-scale  $c_i$ , and the initial weight  $w_i$  of each basis function  $b_i(x, y)$  are shown in Table I. Later on, in our experimental section (Section VIII-E), we can see that those parameter settings can help us to simulate pastureland environments that are very close to the real-world scenario.

### B. Pasture Environment Simulation Results

We simulate a  $10\text{m} \times 10\text{m}$  pasture after careful consideration of the computational speed and complexity of the entire process. To further improve the simulation speed, we divide the pasture into 25 small  $2\text{m} \times 2\text{m}$  patches. For each patch, we use  $1 \times 10^3$  grass models (250 models per square meters). Finally, 25 small patches are attached to form one large  $10\text{m} \times 10\text{m}$  pastureland environment.

We randomly assign grass models and extrude the model in three dimensions to match the predefined height for the model in that location. As the swards of the grass grow with a curvature, we need to adjust the location of the base of each grass model i.e. the location of each individual grass model at the ground plane to match the location of its sward at its highest point. This offset allows us to directly calculate the vertical height of each individual plant. Specifically, denote by  $\gamma \in \mathbb{R}$  the scaling factor of a grass model, which is calculated by comparing the desired height of a grass model and the original height. We denote  $\mathbf{m} = [m_x, m_y]^\top \in \mathbb{R}^2$  the original

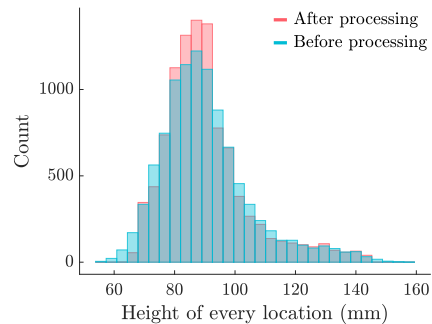


**Fig. 10** The histogram comparison of the two heightmaps shown in Fig. 9.

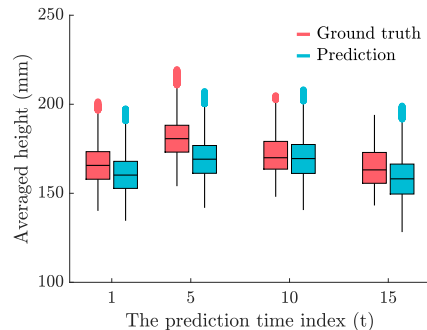


**Fig. 11** The averaged height comparison between the ground truth and the prediction for different prediction time index with  $\alpha = 1, 5, 10, 15$ . Since the time interval is  $\delta = 4$ , the effective prediction length are 4, 20, 40, and 60 days.

2D location of the topmost point, and  $\xi = [\xi_x, \xi_y]^\top \in \mathbb{R}^2$  the offset of the topmost point, where  $\xi_x, \xi_y \in \mathbb{R}$  are the offset in  $x$  and  $y$  direction. We apply a shifting process as  $\mathbf{m} \leftarrow \mathbf{m} - \gamma \cdot \xi$  to ensure that the topmost point is at the predefined location. After this adjustment, the 2D location of the topmost point of a grass model is transformed to the predefined 2D location.

Following the steps described in Section VII, we generate 15 pastureland environments in Gazebo using the historical data with a day interval of  $\delta = 4$ . An example illustrating the simulated pastureland environment ( $10\text{m} \times 10\text{m}$ ) is shown in Fig. 6. In this simulated pastureland environment, there are  $2.5 \times 10^4$  grass models.

Next, we use a robot to collect a point cloud for each of the simulated environments. The simulated LiDAR has an inherent standard deviation of 4mm in its readings. We also assume the ground of the field is flat. Nevertheless, it is easy to add different terrains to simulate different types of ground. During the simulations, the plant locations, pose, and plant species for a particular location in the pasture are fixed throughout the years to accelerate those processes. Finally, all the collected point clouds will be used as testing inputs.

### C. Neural Network Prediction Results

*Training:* In the experiments, the training sequences  $\mathcal{X}_i$ 's are generated by setting the number of measurements in each sequence as  $\alpha = 15$ . Also, the number of intervals is  $\delta = 4$ . Note that the training data is generated through the GMM process defined in earlier sections. We use early stopping

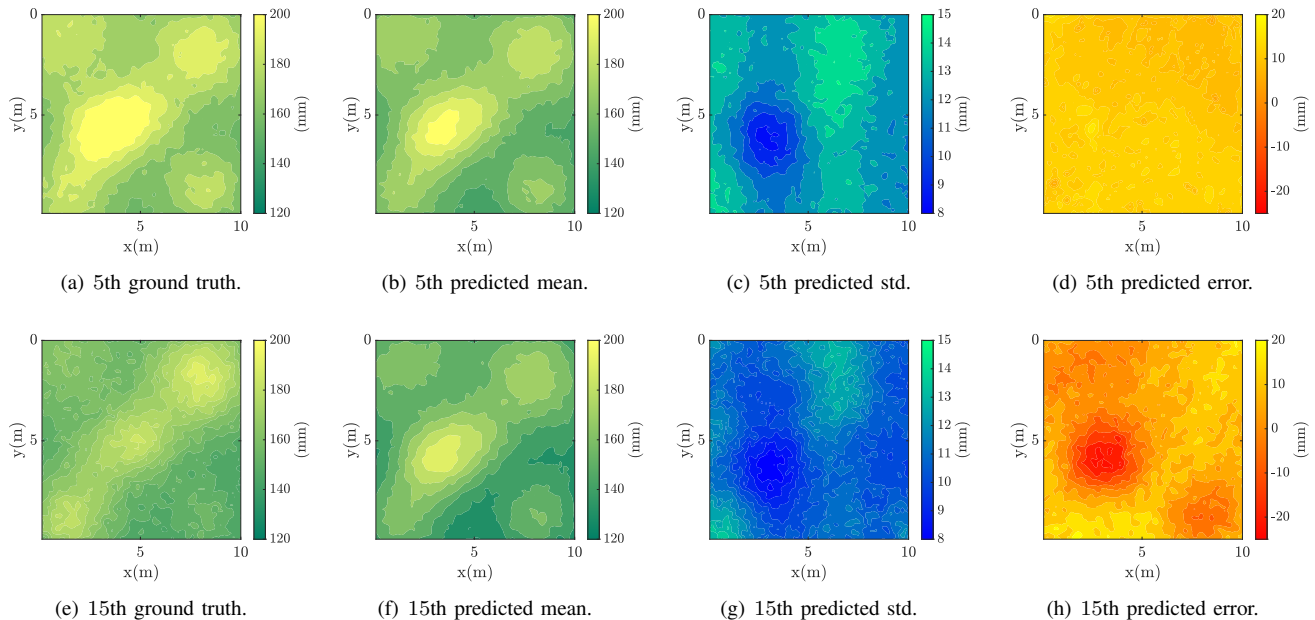


**Fig. 12** The comparison between deep learning predictions and the corresponding ground truth. The first row is for  $\alpha = 5$  prediction (the effective horizon is 40 days), and the second row is for  $\alpha = 15$  prediction (the effective horizon is 60 days). The comparisons include predicted mean, predicted standard deviation, and the prediction error for every location.

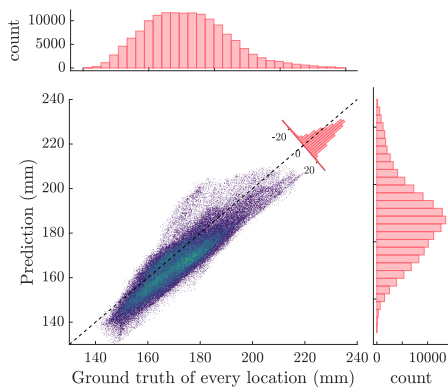


**Fig. 13** The relationship between the ground truth and the corresponding prediction by using all the predictions and the ground truth. The x-axis represents the ground truth of every point, and the y-axis represents the corresponding prediction result. The marginal histograms show the statistics of the ground truth and the prediction independently.

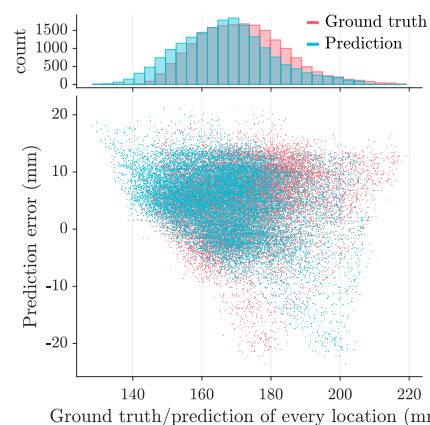


**Fig. 14** The comparison between ground truth/prediction and the corresponding prediction errors of every location.

where training is stopped if validation loss does not improve for ten epochs, usually resulting in 30 training epochs.

*Experimental Evaluation:* We evaluate the performance of the prediction network on two separate cases: a). The first test case is on the aforementioned point cloud measurements; b). The second evaluation is on two years of the simulated GMM data.

*Testing by using point cloud measurements:* We note that due to the computationally intensive process of constructing aforementioned pastures and its subsequent point cloud measurements, we only generate a single test case consisting of 30 days, where the data is split into 15 days as an input sequence to the prediction network, and the remaining 15 days are used to evaluate the prediction performance. The

collected point clouds will be first converted to heightmaps of size  $100 \times 100$  as the original point clouds are too large to be used as network prediction inputs. Meanwhile, we need to process those heightmaps since the measurements are noisy. In Fig. 8, we demonstrate a downsampled surface of the point cloud shown in Fig. 7. Specifically, after downsampling, the processing includes two steps: (a). a size of  $3 \times 3$  median filtering; (b). a size of  $3 \times 3$  flat convolution filtering. After processing, we see that the growth pattern of the pastureland is visible as shown in Fig. 9(b) when compared with the raw map as shown in Fig. 9(a). Those processes make the neural networks' prediction of the dynamics of the pastureland more efficient. Meanwhile, this processing only has mild change on the original data, as can be seen from the histogram comparison in Fig. 10.



**TABLE II** Accuracy metrics (in mm) for different methods with and without uncertainty estimates (UE), where the stride length is  $\delta = \{1, 4\}$  and the cardinality of horizons set is  $\alpha = 15^*$ .

Model	(GMM Data)				(Point Cloud Data)			
	RMSE	MAE	MPAE	ASTD	RMSE	MAE	MPAE	ASTD
$\delta = 4 + \text{UE}$	19.25	13.42	11.91	9.27	<b>7.41</b>	<b>6.46</b>	<b>3.672</b>	12.39
$\delta = 1 + \text{UE}$	<b>6.91</b>	<b>5.12</b>	<b>4.65</b>	<b>8.31</b>	–	–	–	–
$\delta = 4$	24.65	18.79	15.62	–	19.31	18.07	10.58	–
$\delta = 1$	18.52	14.38	13.13	–	–	–	–	–

\* (Since the tests without UE do not implement MC Dropout methods, no ASTD values are available. Additionally, due to high computation requirements for point cloud data, results for  $\delta = 1$  are unavailable.)

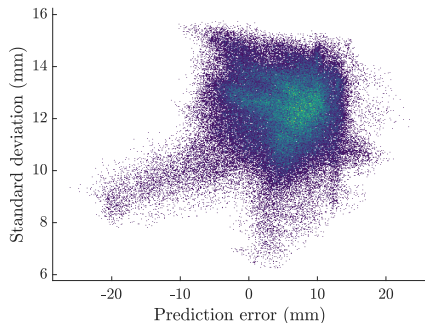


**Fig. 15** The relationship between the prediction error and the corresponding prediction standard deviation of every location by using all the predictions.

To test the prediction performance, we predict the heightmaps for another 15 days using a stride length of  $\delta = \{1, 4\}$ . The longest effective horizon for those two are  $L = 15$  and  $L = 60$  respectively. Then, we generate the corresponding point cloud measurement to check the testing performance. To estimate the uncertainties, we set the number of MC dropout samples as  $K = 500$ . In general, our network performance on average performs within a 12% error rate in the worst case when  $\delta = 4$  and  $L = 60$ , and within a 5% error rate when data is available more frequently when  $\delta = 1$  and  $L = 15$ . In Fig. 11, we plot the comparison between the ground truth and the prediction when the prediction time index  $\alpha = 1, 5, 10$ , and 15 using a stride length of  $\delta = 4$ . The empirical results show that the proposed method performs sufficiently well in predicting and reconstructing pasture heights, even for long-horizon ( $L = 60$  days) problems. To further demonstrate the details of our long-time horizon prediction results, we show the 5th and 15th prediction results with their ground truth in Fig. 12.

Note that the effective time horizons for those two predictions are  $L = 40$  and 60 days. The uncertainty estimations in terms of standard deviations of the predictions run over  $K = 500$  samples, and we observe that the network has higher confidence at the highest pasture heights since it is easier to learn feature mappings due to larger correlations within its neighborhood. The prediction error is lowest at the highest points in the pasture since the network learns to estimate the peak points with higher confidence.

In Fig. 13, we compare the ground truth and the corresponding predictions using all the predictions across the output sequence. From the result, we can see that most prediction-ground truth pairs lie in the 45 degree line, where we can clearly

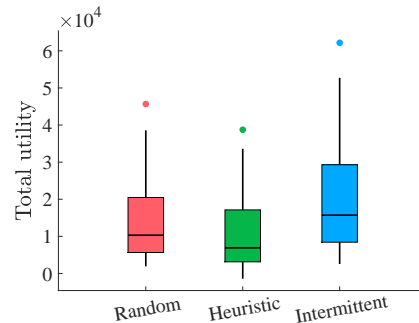


**Fig. 16** The utility statistics of the three methods after running 50 trials. The proposed intermittent deployment method has the highest averaged utility.

observe that most predictions are close to the ground truth. In Fig. 14, we demonstrate the relationship between the prediction errors and the ground truth/prediction for each location, which reinforces the performance of the neural network, where we observe the predictions are quite close to the ground truth. The prediction uncertainty of the model increases as the prediction error increases, as shown in Fig. 15, showing a clear correlation between the confidence of the network against the prediction errors. This reiterates the suitability of the computationally efficient Bayesian approximation for uncertainty estimates, allowing a quick and efficient turnaround in prediction. This methodology reduces the need for expensive hardware for training and inference of the deep learning-based prediction model and allows even small industries or farms to tune and integrate the prediction systems into their workflow.

*Remark 8.1:* Note that in the above tests, the network makes predictions generated from point cloud measurements, and the original training dataset of pasture height maps generated from GMM is not used. This indicates the ability of our network to generalize beyond the simulated training data to real-world applications by using LIDAR-based measurements.

*Testing by using GMM data:* Next, we use Monte Carlo simulations to test the prediction performance using different GMM inputs. Note that the training model is unchanged in this case. We set  $|\mathcal{T}_y| = \alpha = 15$ . That is, we use a length of 15 heightmaps to predict another group of 15 heightmaps. Since we will test the performance using two years' data and the first 15 heightmaps can only be used as inputs, the number of distinct output prediction sequences is  $H = (365 - |\mathcal{T}_y|) \cdot 2$ . We should also note that  $K$  in (4) is the number of samples used for calculating one prediction  $\hat{\mathbf{Y}}_t, \forall t \in \mathcal{T}_y$ . We



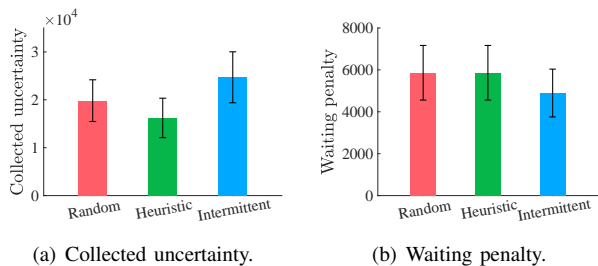


**Fig. 17** (a). The comparison of the collected uncertainties of three different methods, which is the first part of the objective function. (b). The waiting penalty of three different methods, which is the second part of the objective function.

evaluate the performance of the neural network predictions with the following metrics: Root Mean Square Error (RMSE), Mean Absolute Error (MAE), Mean Absolute Percentage Error (MAPE), and Averaged Standard Deviation (ASTD).

$$\begin{aligned} \text{RMSE} &= \sqrt{\frac{1}{H} \sum_{h=1}^H \sum_{t \in \mathcal{T}_y} (\mathbf{Y}_t^{(h)} - \bar{\mathbf{Y}}_t^{(h)})^2}, \\ \text{MAE} &= \frac{1}{H} \sum_{h=1}^H \sum_{t \in \mathcal{T}_y} \left| \mathbf{Y}_t^{(h)} - \bar{\mathbf{Y}}_t^{(h)} \right|, \\ \text{MAPE} &= \frac{100}{H} \sum_{h=1}^H \sum_{t \in \mathcal{T}_y} \left| \frac{\mathbf{Y}_t^{(h)} - \bar{\mathbf{Y}}_t^{(h)}}{\mathbf{Y}_t^{(h)}} \right|, \\ \text{ASTD} &= \sqrt{\frac{1}{H} \sum_{h=1}^H \sum_{t \in \mathcal{T}_y} (\bar{\sigma}_t^{(h)})^2}, \end{aligned}$$

where  $\mathbf{Y}_t^{(h)}$  is the  $h$ th prediction at time  $t$ , and  $\bar{\sigma}_t^{(h)}$  is the corresponding standard deviation. Note that the each mean prediction  $\bar{\mathbf{Y}}_t$  is calculated by using  $K = 500$  samples, i.e.,  $\bar{\mathbf{Y}}_t = \frac{1}{K} \sum_{t=1}^K \hat{\mathbf{Y}}_t$ . The results of these metrics are reported in Table II, containing the results from the above two testings. These metrics quantify the performance of the prediction algorithm by aggregating the errors and uncertainty over the discretized values of the pasture.

#### D. Pipeline Comparison Results

In this section, we use Monte Carlo simulations to test the performance of the proposed integrated pipeline with another pipeline for sensing and deployment purposes based on GMM data. The size of the heightmaps used for the plannings will be  $100 \times 100$  as before. Specifically, we have two goals for the testings: (a). we want to test the effectiveness of the proposed pipeline when the deployments are different. (b). We want to test the effectiveness of the proposed pipeline when the prediction methods are different.

*The first comparison:* Based on the same deep learning prediction result, we compare the performance using the following deployment policies:

- The intermittent deployment policy, where the policy is generated through the method proposed in Section VI. We refer to this policy as “Intermittent”.

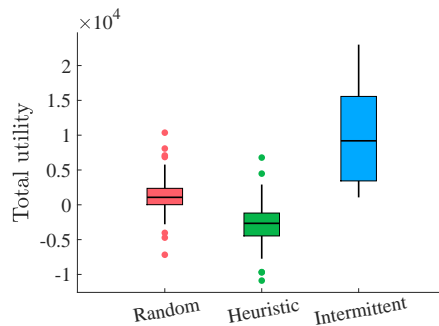


**Fig. 18** The utility statistics of the three methods after running 50 trials when the waiting penalty weight  $w_1$  is high.

- A fixed interval deployment policy, where the robots are deployed within a fixed time interval. Also, the deployment locations are evenly distributed across the pastureland (mimicking how humans manually monitor pasturelands). We refer to this policy as “Heuristic”.
- A random deployment policy, where both deployment times and locations are randomly selected from the ground set  $\mathcal{V}$ . We refer to this policy as “Random”.

We first evaluate the performance using the collected reward (the objective function value). Then, we collect samples based on the generated deployment policies. After that, we use the collected information from different methods to make 10 more predictions. We finally compare the prediction performance of those methods. Thus, those steps will help verify the proposed pipeline’s effectiveness.

*The second comparison:* We adopt a commonly used mutual information-based pipeline in the second comparison category and compare it with our proposed pipeline. Specifically, we will use a 2D Gaussian process (GP) to model the environment and make predictions. We then use the proposed intermittent deployment idea to make deployment strategies based on the different prediction results. Again, we finally make another 10 future predictions after deployments to test the performance.

*The results from the first comparison:* Based on the  $\alpha = 15$  deep learning prediction results, we run 50 Monte Carlo simulations to generate different deployments under different settings. The settings are as follows. The maximum number of deployable days (total budget)  $\ell$  is randomly sampled from the set  $\{5, 6, \dots, 12\}$ . The number of maximum sampling points  $\ell_t$  is sampled from the set  $\{2^2, 3^2, \dots, 8^2\}$ . The cardinality of the planning horizon is  $|\mathcal{T}_y| = 15$ . We also assign each robot a random weight for the same traveling cost to simulate the heterogeneity. In each run, we generate one instance and then use the above three methods to compare the performance. Also, the number of robots is set to  $\ell_t \cdot \ell$  for each instance. The weights for distance and time are  $w_2 = 0.1, w_3 = 1$ . And the weight for time penalty is  $w_1 = 5$ . The definitions of those parameters can be found in our problem formulation in Section III-B.

Then, we first compare the results of different deployment policies by comparing the collected reward of each method after running 50 trials. The result is shown in Fig. 16, where the proposed intermittent policy has the highest averaged utility.

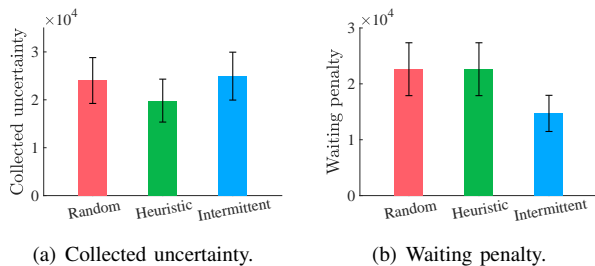


**Fig. 19** The utility/cost of different parts of our objective function when the waiting penalty weight  $w_1$  is high.

**TABLE III** The averaged prediction comparisons (in mm) between the deep learning (DL) based method and the Gaussian process (GP) for  $\alpha = 5$  and  $\alpha = 15$ .

Time	Truth	(DL prediction)		(GP prediction)	
		Prediction	Error	Prediction	Error
$\alpha = 5$	181.53	169.82	<b>11.71</b>	149.87	31.66
$\alpha = 15$	164.42	158.83	<b>5.60</b>	117.08	47.34

Then, in Fig. 17, we demonstrate the two different parts of the objective function. In Fig. 17(a), we show the collected uncertainty of three different deployment methods, which is the first part of the objective function. In Fig. 17(b), we compare the waiting penalty part in the objective function. Then, in Fig. 18, we set a high waiting penalty as  $w_1 = 10$  while keeping  $w_2, w_3$  the same as before. Again, we run other 50 trials to compare the performance. In Fig. 18, the values of different parts in the objective function prove that our proposed method can collect more rewards while having less waiting penalty. Similarly, in Fig. 19, we compare the result from each part of the objective function using three different deployment policies. This finishes up the first part of this comparison. In Fig. 20, we demonstrate a deployment result using one setting instance. In this result, we set the parameters as follows. The maximum number of deployments for each day is set to  $\ell_t = 4$ , and the maximum number of deployable days is set to  $\ell = 3$ .

Next, we use robots to collect data based on the generated deployment policies. The collected height information will be used to update our knowledge of the environment. Finally, we compare the predictions from each method using this updated information. Note that white noise is also added to simulate measurement noise. Specifically, we use the collected information to make another 10 more predictions, i.e., from  $\alpha = 1$  to  $\alpha = 10$ , with the size of interval of  $\delta = 2$ . For each prediction, we compare it with the ground truth. Then, the final averaged prediction error is shown in Fig. 21. The averaged prediction error is calculated by averaging the prediction errors from all locations. Since we run the simulation 50 trials, there are 50 different averaged prediction errors for each method shown in Fig. 21. We see that the proposed pipeline has a lower averaged prediction error than the other two methods after using the updated information from different methods. This demonstrates the effectiveness of the proposed method.

*The results from the second comparison:* In this comparison, we first use GP to make predictions. The settings of this GP

**TABLE IV** The statistics of the averaged prediction errors of the proposed deep learning (DL) based pipeline and the Gaussian process (GP) based pipeline using 50 trials.

	Mean (mm)	Std. (mm)
DL based pipeline	<b>11.39</b>	<b>0.08</b>
GP based pipeline	36.09	0.21

are as follows. The training dataset is from the point clouds generated in Gazebo as described in Section VII. We also need to convert those point clouds into heightmaps. We denote the training inputs of the GP by  $\mathbf{x}_t = [x, y, t] \in \mathbb{R}^3$ . The training outputs are corresponding grass height of location  $(x, y)$  at time  $t$ . From the above 15 heightmaps, we randomly pick  $1 \times 10^3$  points across all those heightmaps to form the training set. Since GP is a non-parametric method, we select kernels as follows. The mean kernel is defined using the historical mean data as shown in Fig. 5. The covariance kernel is a composite of a 2D Gaussian covariance kernel and a 1D linear covariance kernel with noise term. The Gaussian covariance kernel is similar to the one shown in (3). Then, those two covariance kernels are summed up to form the final covariance kernel. In Fig. 22, we show two prediction results when  $\alpha = 5$  and  $\alpha = 15$ . We notice that the proposed learning-based method can maintain more details than that of the GP based predictions. We also include the comparison details of those two comparisons in Table III. Note that the comparison is based on the averaged prediction errors.

Next, we use the proposed intermittent deployment method to select measurement locations based on the mutual information while respecting the proposed constraints (7) and (8). Note that the mutual information matrix is build on all the available locations at different times. The parameters and the settings are the same as described in the first comparison. We then run 50 trials using those settings to generate different deployment policies. Since the mutual information-based method requires a full covariance matrix for the deployment ground set  $\mathcal{V}$ , which is extremely computational expensive, we choose to reduce the original  $100 \times 100$  deployable locations to  $10 \times 10$  deployable locations. Based on the deployment result of each trial, we finally make predictions for the next 10 steps. Therefore, the performance comparison between this mutual information-based pipeline and the proposed pipeline is based on the final prediction results. In Fig. 23 and Fig. 24, we demonstrate the averaged prediction error of each pipeline. Also, the statistics of this comparison are shown in Table IV.

### E. Perception Results

In this section, we demonstrate the result from a field experiment to illustrate the effectiveness of our simulated pastureland environment.

We experimented at Virginia Tech’s Turfgrass Research Center to test out our growth analysis algorithm. A  $10\text{m} \times 10\text{m}$  region of the Turfgrass center was reserved, and the grass was grown. It was untouched over time, but the perimeter around it was consistently mowed down. A DJI M600 UAV with a bottom-facing Velodyne VLP-16 3D-LiDAR, as shown in Fig. 25, was flown over the region. The localization information

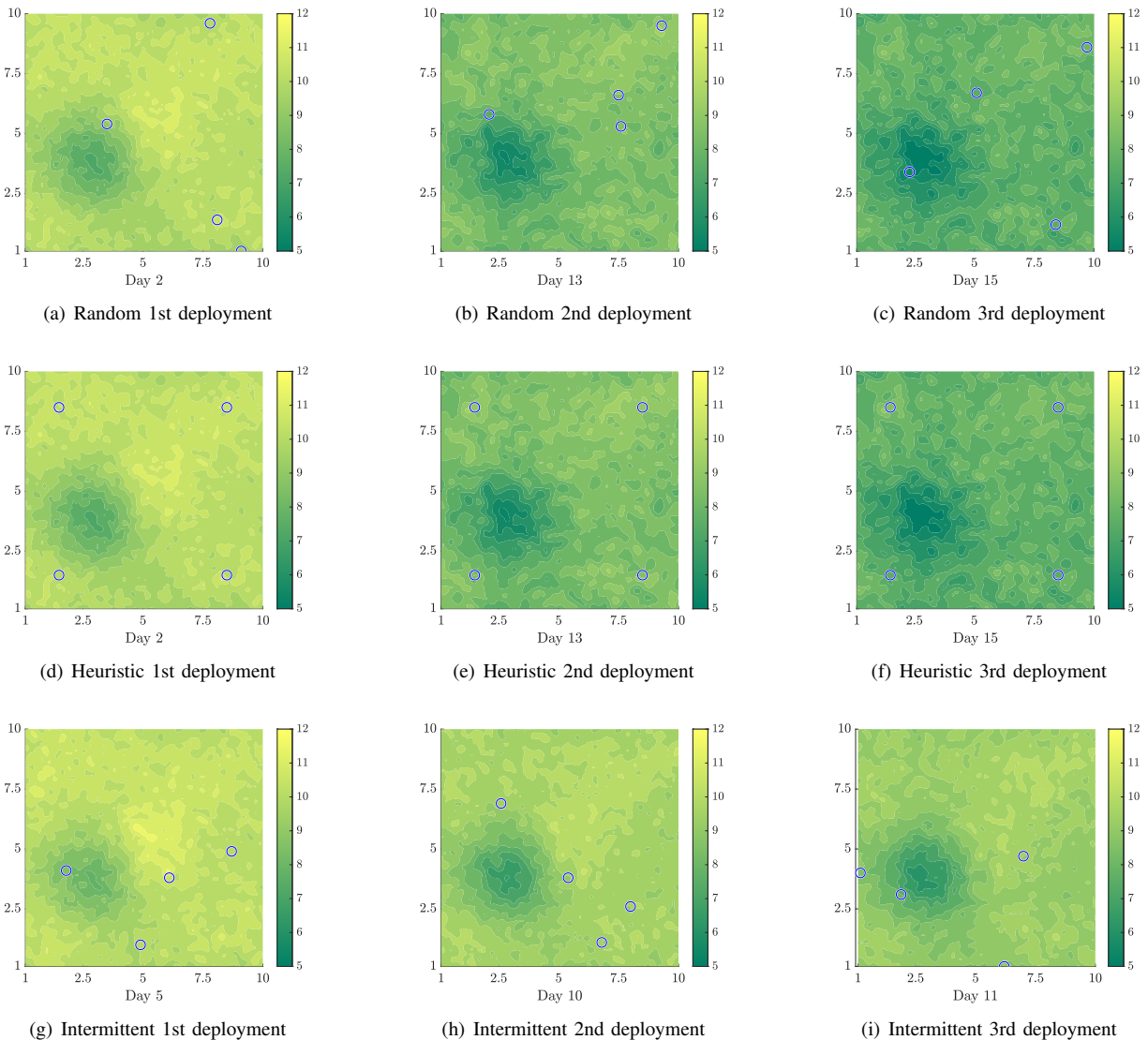


**Fig. 20** An example of deployment policies generated by different methods. (a)-(c). random, (d)-(f). heuristic, (g)-(i). intermittent. Those are predicted variance maps.

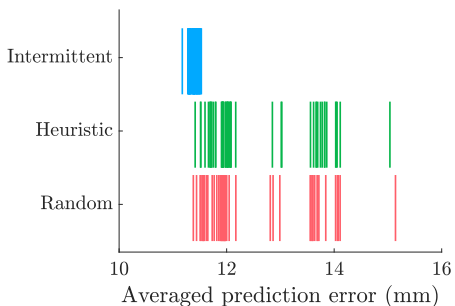


**Fig. 21** The comparison of the averaged prediction error by calculating the mean of the errors at each location using 50 trials.

and LiDAR scans during flights were collected using an onboard NVIDIA Jetson TX2. This data was used to build a point cloud map of the region using a similar technique to

**TABLE V** Turfgrass experiment heights.

	Week 1	Week 2	Week 3	Week 4
Hand Measurement	48.00 cm	68.17 cm	74.11 cm	69.04 cm
50th Percentile	3.97 cm	10.67 cm	12.17 cm	9.60 cm
75th Percentile	6.31 cm	16.01 cm	18.41 cm	14.60 cm
90th Percentile	8.73 cm	22.08 cm	26.11 cm	19.93 cm
95th Percentile	11.03 cm	27.48 cm	31.53 cm	24.49 cm
97.5th Percentile	13.43 cm	32.22 cm	36.64 cm	30.43 cm
99th Percentile	15.63 cm	36.43 cm	41.65 cm	36.17 cm
99.5th Percentile	16.70 cm	39.23 cm	44.29 cm	39.42 cm

the one used in the point cloud generation for the simulation discussed previously. These flights were conducted weekly to get temporal point cloud maps of the region. Manual measurements of the region were also collected. Nine spots throughout the region were used as the manual measurement points. These were averaged to get the manual measurements shown in Table V.

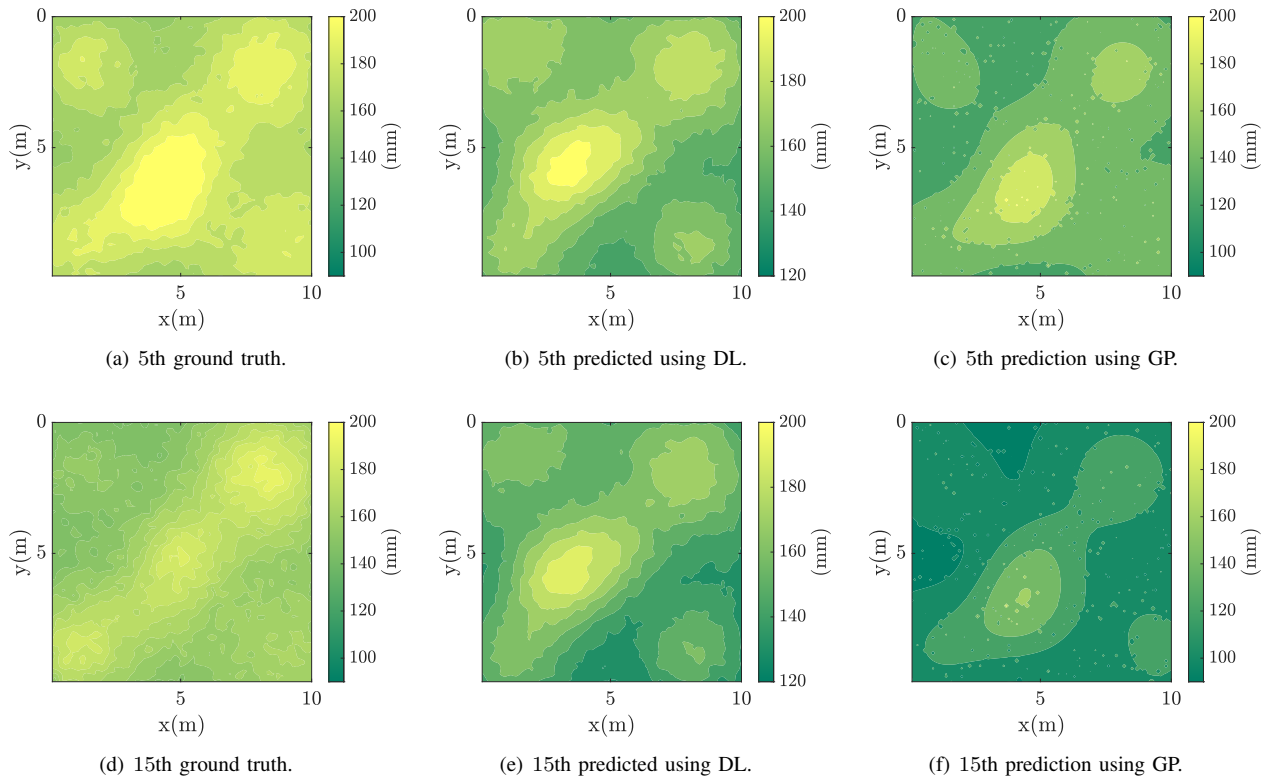


**Fig. 22** The comparison between the ground truth and the predictions by using deep learning (DL) based method and Gaussian process (GP) based method.

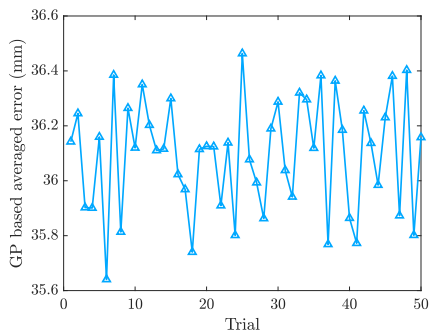


**Fig. 23** The averaged prediction errors using Gaussian process (GP) and mutual information based pipeline after 50 trials.

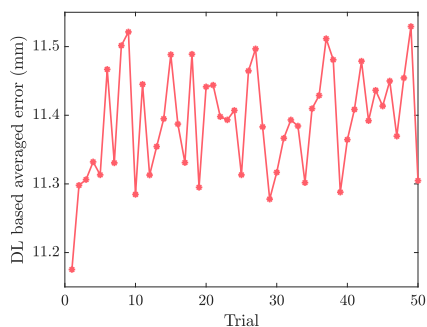


**Fig. 24** The averaged prediction errors using the proposed deep learning (DL) based pipeline after 50 trials.

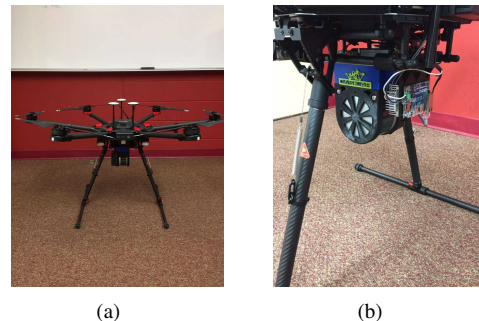


**Fig. 25** A UAV (DJI M600) mounted with a LiDAR (Velodyne VLP-16) and an onboard system (Nvidia Jetson TX2).

**TABLE VI** Turfgrass experiment growth.

	Week 1-2	Week 2-3	Week 3-4
Hand Measurement	20.17 cm	5.94 cm	-5.07 cm
50th Percentile	6.72 cm	1.49 cm	-2.58 cm
75th Percentile	9.70 cm	2.40 cm	-3.81 cm
90th Percentile	13.34 cm	4.03 cm	-6.18 cm
95th Percentile	16.45 cm	4.05 cm	-7.05 cm
97.5th Percentile	18.79 cm	4.40 cm	-6.21 cm
99th Percentile	20.80 cm	5.22 cm	-5.48 cm
99.5th Percentile	22.54 cm	5.05 cm	-4.87 cm

The distance between every point in the region's point cloud and the ground plane was computed to estimate the height of these points. This was done using the normal vector determined using the method described Section VII. Because the vast



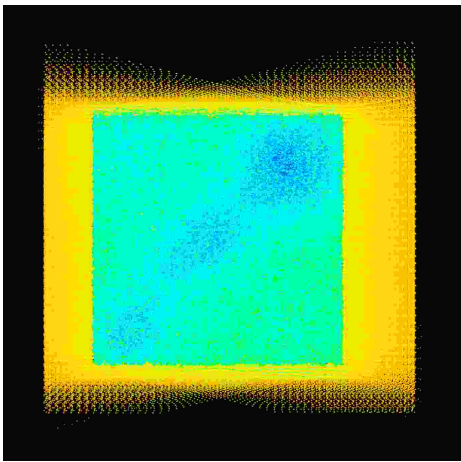


**Fig. 26** Unprocessed point cloud of  $10 \times 10$  meter Turfgrass plot with the perimeter. The UAV flew over the generated plot in the simulation. The data collected from the 3D LiDAR is shown in this figure. The yellow points are the perimeter around the plot, and the blue/green points are the points in the plot. With the plot being taller, the points registered were closer. The bluer the point, the closer it is.

majority of LiDAR points were not at the very top of the grass, the height estimations using this method were underestimations regardless of which percentile we looked at. This is shown in Table V, and the result is shown in Fig. 26. However, since growth is what we are looking into, we can look at the relative differences in the estimations between each flight. These differences are shown in Table VI with the first row showing the manually measured growth between sampling weeks. With perfect estimations, the percent difference between the manual measurements and estimated height would be 0%. However, our best results were found using the 99th percentile of growth estimates which had an average percent difference of 7.9% compared to manual measurements.

Those real-world experiments shown above validate our pasture simulation regime and thus our evaluation results. Meanwhile, the point cloud results from the real-world experiments are close to the results in our simulated world. All those results demonstrate the effectiveness of our proposed pipeline.

## IX. CONCLUSIONS AND FUTURE WORK

In this work, we proposed an integrated pipeline that can be used for long-term, large-scale forage perception applications. From the perspective of simulation, we demonstrated how to simulate large pastureland environments reasonably fast using parallel processing. From the perspective of pasture prediction, we proposed a new deep learning architecture that can be used for long-term pasture predictions. From the perspective of perception, we demonstrated how to get accurate pasture height estimation through regression. From the perspective of autonomy, we combined predictions and an intermittent deployment policy to deploy robots with high accuracy while at low cost.

This work resulted in novel approaches from the initial data-generating to the final deployment testing. The proposed pipeline offers a promising and cost-effective alternative to real-life experiments and can be used as a platform for other testings.

## REFERENCES

- [1] J. Bengtsson, J. M. Bullock, B. Egoh, C. Everson, T. Everson, T. O'Connor, P. J. O'Farrell, H. G. Smith, and R. Lindborg, "Grasslands—more important for ecosystem services than you might think," *Ecosphere*, vol. 10, no. 2, pp. 1–20, 2019.
- [2] R. L. Kallenbach, "Describing the dynamic: Measuring and assessing the value of plants in the pasture," *Crop Science*, vol. 55, no. 6, p. 2531–2539, 2015.
- [3] J. Y. L. Tay, A. Erfmeier, and J. M. Kalwij, "Reaching new heights: can drones replace current methods to study plant population dynamics?" *Plant Ecology*, vol. 219, no. 10, p. 1139–1150, Oct 2018.
- [4] K. R. Harmoney, K. J. Moore, J. R. George, E. C. Brummer, and J. R. Russell, "Determination of pasture biomass using four indirect methods," *Agronomy Journal*, vol. 89, no. 4, p. 665–672, Jul 1997.
- [5] L. Heintzman, A. Hashimoto, N. Abaid, and R. K. Williams, "Anticipatory planning and dynamic lost person models for Human-Robot search and rescue," in *2021 IEEE International Conference on Robotics and Automation (ICRA)*. ieeexplore.ieee.org, May 2021, pp. 8252–8258.
- [6] R. K. Williams, N. Abaid, J. McClure, N. Lau, L. Heintzman, A. Hashimoto, T. Wang, C. Patnayak, and A. Kumar, "Collaborative multi-robot multi-human teams in search and rescue," *Proceedings of the International ISCRAM Conference*, vol. 17, Apr. 2020.
- [7] "Gazebo simulator," <http://gazebo.org>.
- [8] D. P. Holzworth, N. I. Huth, P. G. deVoil, E. J. Zurcher, N. I. Herrmann, G. McLean, K. Chenu, E. J. van Oosterom, V. Snow, and C. Murphy, "APSIM—evolution towards a new generation of agricultural systems simulation," *Environmental Modelling & Software*, vol. 62, p. 327–350, 2014.
- [9] M. T. Schaefer and D. W. Lamb, "A combination of plant NDVI and LiDAR measurements improve the estimation of pasture biomass in tall fescue (*Festuca arundinacea* var. *fletcheri*)," *Remote Sensing*, vol. 8, no. 22, p. 109, Feb 2016.
- [10] M. Rangwala, J. Liu, K. S. Ahluwalia, S. Ghajar, H. S. Dhami, B. F. Tracy, P. Tokekar, and R. K. Williams, "DeepPaSTL: Spatio-temporal deep learning methods for predicting long-term pasture terrains using synthetic datasets," *Agronomy*, vol. 11, no. 11, p. 2245, 2021.
- [11] A. Schrijver, *Combinatorial optimization: polyhedra and efficiency*. Springer Science & Business Media, 2003, vol. 24.
- [12] J. G. Oxley, *Matroid theory*. Oxford University Press, USA, 2006, vol. 3.
- [13] R. N. Smith, M. Schwager, S. L. Smith, B. H. Jones, D. Rus, and G. S. Sukhatme, "Persistent ocean monitoring with underwater gliders: Adapting sampling resolution," *Journal of Field Robotics*, vol. 28, no. 5, pp. 714–741, 2011.
- [14] S. McCammon, G. Marcon dos Santos, M. Frantz, T. Welch, G. Best, R. K. Shearman, J. D. Nash, J. A. Barth, J. A. Adams, and G. A. Hollinger, "Ocean front detection and tracking using a team of heterogeneous marine vehicles," *Journal of Field Robotics*, 2021.
- [15] S. Asseng, F. Ewert, C. Rosenzweig, J. W. Jones, J. L. Hatfield, A. C. Ruane, K. J. Boote, P. J. Thorburn, R. P. Rötter, D. Cammarano, and et al., "Uncertainty in simulating wheat yields under climate change," *Nature Climate Change*, vol. 3, no. 9, p. 827–832, Sep 2013.
- [16] F. Li, P. Newton, and M. Lieffering, "Testing simulations of intra- and inter-annual variation in the plant production response to elevated CO<sub>2</sub> against measurements from an 11-year face experiment on grazed pasture," *Global change biology*, vol. 20, Aug 2013.
- [17] G. R. Balboa, S. V. Archontoulis, F. Salvagiotti, F. O. Garcia, W. M. Stewart, E. Francisco, P. V. V. Prasad, and I. A. Ciampitti, "A systems-level yield gap assessment of maize-soybean rotation under high- and low-management inputs in the western us corn belt using APSIM," *Agricultural Systems*, vol. 174, p. 145–154, Aug 2019.
- [18] R. M. Jones, R. J. Jones, and C. K. McDonald, "Some advantages of long-term grazing trials, with particular reference to changes in botanical composition," *Australian Journal of Experimental Agriculture*, vol. 35, no. 7, p. 1029–1038, 1995.
- [19] M. S. Corson, R. H. Skinner, and C. A. Rotz, "Modification of the spur rangeland model to simulate species composition and pasture productivity in humid temperate regions," *Agricultural Systems*, vol. 87, no. 2, p. 169–191, Feb 2006.
- [20] R. H. Mohtar, T. Zhai, and X. Chen, "A world wide web-based grazing simulation model (GRASIM)," *Computers and Electronics in Agriculture*, vol. 29, no. 3, p. 243–250, Dec 2000.
- [21] C. A. Rotz and U. S. Gupta, "Dafosym for windows: A teaching aid in forage system management," in *Proceedings of the American Forage and Grassland Conference*, 1996.



- [22] D. Holzworth, N. I. Huth, J. Fainges, H. Brown, E. Zurcher, R. Cichota, S. Verrall, N. I. Herrmann, B. Zheng, and V. Snow, "APSIM next generation: Overcoming challenges in modernising a farming systems model," *Environmental Modelling & Software*, vol. 103, p. 43–51, 2018.
- [23] M. Ahmed, D. Parsons, J. Morel, K. Uttam, B. Sandström, M. Lanna, and J. Wallsten, "APSIM next generation to model red clover under nordic climate," in *Proceedings of the International Crop Modelling Symposium*, 2020.
- [24] C. Bosi, P. C. Sentelhas, N. I. Huth, J. R. M. Pezzopane, M. P. Andreucci, and P. M. Santos, "APSIM-tropical pasture: A model for simulating perennial tropical grass growth and its parameterisation for palisade grass (*brachiaria brizantha*)," *Agricultural Systems*, vol. 184, p. 102917, Sep 2020.
- [25] F. Y. Li, V. O. Snow, D. P. Holzworth, and I. R. Johnson, "Integration of a pasture model into APSIM," in *Proceedings of the Australian Agronomy Conference*. Australian Society of Agronomy Inc, 2010, pp. 6–10.
- [26] C. K. Williams and C. E. Rasmussen, *Gaussian processes for machine learning*. MIT press Cambridge, MA, 2006, vol. 2, no. 3.
- [27] J. Liu and R. K. Williams, "Data-driven models with expert influence: A hybrid approach to spatiotemporal process estimation," in *Proceedings of the IEEE/RSJ International Conference on Intelligent Robots and Systems*, 2020, pp. 2467–2473.
- [28] M. Oliu, J. Selva, and S. Escalera, "Folded recurrent neural networks for future video prediction," in *Proceedings of the European Conference on Computer Vision*, 2018, pp. 716–731.
- [29] S. Hochreiter and J. Schmidhuber, "Long short-term memory," *Neural computation*, vol. 9, no. 8, pp. 1735–1780, 1997.
- [30] A. Graves, "Generating sequences with recurrent neural networks," *arXiv preprint arXiv:1308.0850*, 2013.
- [31] M. Rangwala and R. Williams, "Learning multi-agent communication through structured attentive reasoning," in *Proceedings of the Advances in Neural Information Processing Systems*, vol. 33, 2020, pp. 10088–10098.
- [32] V. Michalski, R. Memisevic, and K. Konda, "Modeling deep temporal dependencies with recurrent grammar cells," in *Proceedings of the Advances in neural information processing systems*, vol. 27, 2014, pp. 1925–1933.
- [33] N. Srivastava, E. Mansimov, and R. Salakhudinov, "Unsupervised learning of video representations using lstms," in *Proceedings of the International conference on machine learning*. PMLR, 2015, pp. 843–852.
- [34] S. Xingjian, Z. Chen, H. Wang, D.-Y. Yeung, W.-K. Wong, and W.-c. Woo, "Convolutional LSTM network: A machine learning approach for precipitation nowcasting," in *Proceedings of the Advances in neural information processing systems*, 2015, pp. 802–810.
- [35] W. Lotter, G. Kreiman, and D. Cox, "Deep predictive coding networks for video prediction and unsupervised learning," *arXiv preprint arXiv:1605.08104*, 2016.
- [36] R. Villegas, J. Yang, S. Hong, X. Lin, and H. Lee, "Decomposing motion and content for natural video sequence prediction," *arXiv preprint arXiv:1706.08033*, 2017.
- [37] Y. Wang, M. Long, J. Wang, Z. Gao, and P. S. Yu, "Predrnn: Recurrent neural networks for predictive learning using spatiotemporal lstms," in *Proceedings of the International Conference on Neural Information Processing Systems*, 2017, pp. 879–888.
- [38] Y. Wang, Z. Gao, M. Long, J. Wang, and S. Y. Philip, "Predrnn++: Towards a resolution of the deep-in-time dilemma in spatiotemporal predictive learning," in *Proceedings of the International Conference on Machine Learning*. PMLR, 2018, pp. 5123–5132.
- [39] R. M. Neal, *Bayesian learning for neural networks*. Springer Science & Business Media, 2012, vol. 118.
- [40] D. J. MacKay, "A practical bayesian framework for backpropagation networks," *Neural computation*, vol. 4, no. 3, pp. 448–472, 1992.
- [41] J. Paisley, D. Blei, and M. Jordan, "Variational bayesian inference with stochastic search," *arXiv preprint arXiv:1206.6430*, 2012.
- [42] D. P. Kingma and M. Welling, "Auto-encoding variational bayes," *arXiv preprint arXiv:1312.6114*, 2013.
- [43] D. J. Rezende, S. Mohamed, and D. Wierstra, "Stochastic backpropagation and approximate inference in deep generative models," in *Proceedings of the International conference on machine learning*. PMLR, 2014, pp. 1278–1286.
- [44] M. D. Hoffman, D. M. Blei, C. Wang, and J. Paisley, "Stochastic variational inference," *Journal of Machine Learning Research*, vol. 14, no. 5, 2013.
- [45] Y. Gal and Z. Ghahramani, "Dropout as a bayesian approximation: Representing model uncertainty in deep learning," in *Proceedings of the International conference on machine learning*. PMLR, 2016, pp. 1050–1059.
- [46] P. Baldi and P. J. Sadowski, "Understanding dropout," in *Proceedings of the Advances in neural information processing systems*, vol. 26, 2013, pp. 2814–2822.
- [47] A. Damianou and N. D. Lawrence, "Deep gaussian processes," in *Artificial intelligence and statistics*, 2013, pp. 207–215.
- [48] G. A. Hollinger and S. Singh, "Multirobot coordination with periodic connectivity: Theory and experiments," *IEEE Transactions on Robotics*, vol. 28, no. 4, pp. 967–973, 2012.
- [49] M. Gini, "Multi-robot allocation of tasks with temporal and ordering constraints," in *Proceedings of the AAAI Conference on Artificial Intelligence*, 2017.
- [50] X. Lan and M. Schwager, "Planning periodic persistent monitoring trajectories for sensing robots in gaussian random fields," in *Proceedings of the IEEE International Conference on Robotics and Automation*, 2013, pp. 2415–2420.
- [51] P. Tokekar and V. Kumar, "Visibility-based persistent monitoring with robot teams," in *Proceedings of the IEEE/RSJ International Conference on Intelligent Robots and Systems*, 2015, pp. 3387–3394.
- [52] T. Li, C. Wang, M. Q.-H. Meng, and C. W. de Silva, "Attention-driven active sensing with hybrid neural network for environmental field mapping," *IEEE Transactions on Automation Science and Engineering*, 2021.
- [53] G. A. Hollinger and G. S. Sukhatme, "Sampling-based robotic information gathering algorithms," *The International Journal of Robotics Research*, vol. 33, no. 9, pp. 1271–1287, 2014.
- [54] L. V. Nguyen, S. Kodagoda, R. Ranasinghe, and G. Dissanayake, "Information-driven adaptive sampling strategy for mobile robotic wireless sensor network," *IEEE Transactions on Control Systems Technology*, vol. 24, no. 1, pp. 372–379, 2015.
- [55] Y. Xu, J. Choi, S. Dass, and T. Maiti, "Efficient bayesian spatial prediction with mobile sensor networks using gaussian markov random fields," *Automatica*, vol. 49, no. 12, pp. 3520–3530, 2013.
- [56] J. Liu and R. K. Williams, "Optimal intermittent deployment and sensor selection for environmental sensing with multi-robot teams," in *Proceedings of the IEEE International Conference on Robotics and Automation*, 2018, pp. 1078–1083.
- [57] J. Liu and R. K. Williams, "Submodular optimization for coupled task allocation and intermittent deployment problems," *IEEE Robotics and Automation Letters*, vol. 4, no. 4, pp. 3169–3176, 2019.
- [58] J. Liu and R. K. Williams, "Monitoring over the long term: Intermittent deployment and sensing strategies for multi-robot teams," in *Proceedings of the IEEE International Conference on Robotics and Automation*, 2020, pp. 7733–7739.
- [59] R. K. Williams, A. Gasparri, and G. Ulivi, "Decentralized matroid optimization for topology constraints in multi-robot allocation problems," in *IEEE International Conference on Robotics and Automation*, 2017, pp. 293–300.
- [60] J. Liu and R. K. Williams, "Coupled temporal and spatial environment monitoring for multi-agent teams in precision farming," in *Proceedings of the IEEE Conference on Control Technology and Applications*, 2020, pp. 273–278.
- [61] L. Heintzman and R. K. Williams, "Multi-agent intermittent interaction planning via sequential greedy selections over position samples," *IEEE Robot. Autom. Lett.*, vol. 6, no. 2, pp. 534–541, Apr. 2021.
- [62] R. Wehbe and R. K. Williams, "Optimizing topologies for probabilistically secure multi-robot systems," in *IEEE International Conference on Robotics and Automation*, 2020, pp. 6640–6646.
- [63] R. Wehbe and R. K. Williams, "Probabilistic resilience of dynamic Multi-Robot systems," *IEEE Robotics and Automation Letters*, vol. 6, no. 2, pp. 1777–1784, Apr. 2021.
- [64] A. Krause, A. Singh, and C. Guestrin, "Near-optimal sensor placements in gaussian processes: Theory, efficient algorithms and empirical studies," *Journal of Machine Learning Research*, vol. 9, no. 2, 2008.
- [65] H.-L. Choi, L. Brunet, and J. P. How, "Consensus-based decentralized auctions for robust task allocation," *IEEE transactions on robotics*, vol. 25, no. 4, pp. 912–926, 2009.
- [66] M. Conforti and G. Cornuéjols, "Submodular set functions, matroids and the greedy algorithm: tight worst-case bounds and some generalizations of the rado-edmonds theorem," *Discrete applied mathematics*, vol. 7, no. 3, pp. 251–274, 1984.
- [67] M. L. Fisher, G. L. Nemhauser, and L. A. Wolsey, "An analysis of approximations for maximizing submodular set functions—II," in *Polyhedral combinatorics*. Springer, 1978, pp. 73–87.
- [68] S. Jorgensen, R. H. Chen, M. B. Milam, and M. Pavone, "The matroid team surviving orienteers problem: Constrained routing of heterogeneous teams with risky traversal," in *IEEE/RSJ International Conference on Intelligent Robots and Systems*, 2017, pp. 5622–5629.

- [69] J. Liu, L. Zhou, P. Tokekar, and R. Williams, "Distributed resilient submodular action selection in adversarial environments," *IEEE Robotics and Automation Letters*, 2021.
- [70] S. V. Archontoulis, F. E. Miguez, and K. J. Moore, "Evaluating APSIM maize, soil water, soil nitrogen, manure, and soil temperature modules in the midwestern united states," *Agronomy Journal*, vol. 106, no. 3, p. 1025–1040, 2014.
- [71] P. Hennig, "Animating samples from gaussian distributions," Technical Report 8, Spemannstraße, 72076 Tübingen, Germany: Max Planck, Tech. Rep., 2013.
- [72] O. Ronneberger, P. Fischer, and T. Brox, "U-net: Convolutional networks for biomedical image segmentation," in *Proceedings of the International Conference on Medical image computing and computer-assisted intervention*. Springer, 2015, pp. 234–241.